UNIVERSITAT DE BARCELONA

FACULTY OF PHYSICS

MECHANICAL-OPTICAL-MECHANICAL PHONONIC FREQUENCY COMB GENERATION AT GHZ RANGE

MASTER THESIS

Paul Nizet Ruiz

Under the supervision of:
Dr. Ryan Cecil Ng
Dr. Guilhem Madiot

July 2022

Acknowledgements

I wanted to dedicate some words to the people that made this work possible.
First of all, I want to thank my supervisors Guilhem Madiot and Ryan Ng. They helped me from the very beginning of the internship practicing making fiber loops to the very end in the data processing and interpretation. Thank you for your patience and advice. I would also want to thank all the rest of the Photonic and Phononic Nanostructures Group including the group leader Prof. Clivia Sotomayor and the rest of the group: Emiglio, Omar, Francisco, Martin, Mariana, Peng. and, the visiting members Lisa, my office mate, and Simon. Also thanks to the ICN2 internship grant I had the opportunity to have during the realization of this work. Finally, thanks to the people that indirectly helped me during the thesis and supported me; there will be many to be mentioned within this group.

Contents

Motivation

Light carries momentum which can give rise to radiation pressure forces. The idea of electromagnetic radiation exerting a force onto physical objects was already postulated in the 17th century by Kepler [1], who observed that the tail of comets always point away from the Sun during their transit. This phenomenon is now used for a variety of applications such as the cooling of atomic motion with lasers [2,3], the cooling vibrational motion of mechanical resonators [4–8], and the induction of mechanical oscillations in a system [9, 10]. This lattermost application is in accordance with the work of V.B. Braginsky [11] which predicted that circulating radiation in a Fabry-Pérot cavity could induce a pressure that is able to couple optical modes to the mechanical modes of the structure. Mechanical oscillation generation has significant potential for applications in information processing [12, 13] and data communication. This is because phonons have the possibility to be used as carriers of information signals in the MHz and GHz domain which allows them to connect the operating regimes of electronics and optics [14, 15].
In 2007, P. Del'Haye et al. employed a silica micro-toroid resonator and demonstrated that by coupling the optical modes of the structure to the mechanics of the platform, an equally spaced frequency spectra appeared [16]. This was the first demonstration of the so called Kerr frequency combs, a type of optical comb generated via the Kerr nonlinearity. Frequency combs, more specifically, optical frequency combs have revolutionized the field of frequency metrology and spectroscopy and are enabling components for a variety of applications due to their ability to allow for precise measurement of optical frequencies [17]. Applications include comb-calibration of tunable lasers [18], direct comb spectroscopy [19], arbitrary waveform generation [20], and advanced telecommunications. Although the formation of mechanical combs has also been observed [21–24], they have not received as much attention as their optical counterparts.
The present work presents an optomechanical system based on two phononic crystals with a guided mode around 6.8 GHz placed alongside an air-slot which serves as the optical cavity. A vibrational mode in the MHz has also been reported in the structure. The coupling of an optical mode to the mechanical modes of the structure allows for the amplification of the oscillations in the platform via the radiation pressure force. This Mechanical-Optical-Mechanical (M-O-M) coupling between light and mechanics allows the observation of a phononic periodic spectral feature centered at 6.78 GHz with a width of around 2 GHz when the radiation pressure is increased. This study reports a self-sustained phononic comb formation in the GHz range.

1 Concepts and definitions

This section reviews the fundamentals of cavity optomechanical (OM) systems. Starting from the main variables and equations describing mechanical resonators and optical cavities and radiation pressure definition, the reader will be introduced the principal parameters and behaviours of the optomechanical theory.

1.1 Introduction to mechanical resonators and wave propagation

Most vibrating systems can be modeled as a mechanical oscillator. From **Appendix** A, the behaviour of these kinds of oscillators is described by

$$m_{eff}\frac{d^2x(t)}{dt^2} = -m_{eff}\Omega_m^2 x(t) - m_{eff}\Gamma_m\frac{d}{dt}x(t) + F(t) \tag{1.1}$$

where m_{eff}, Ω_m, and Γ_m, represent the effective mass, resonance frequency, and decay rate of the mechanical resonator, respectively. As such, this equation includes a harmonic oscillator term, a damping term, and an external force.
Different resonators have different responses to the exciting force and, depending on their properties, they oscillate in different manners. The effective mass term m_{eff} allows the description of a structure to be done through this formula treating it as a spring-mass system. The effective mass is not the mass of the resonator itself, but a calculation that depends on the mode displacement profile under study. For a mechanical resonator, the effective mass for the n^{th} mode can be calculated from [25]

$$m_{\text{eff},n} = \int dV\,\rho(\mathbf{x})\,|\mathbf{r}_n(x)|^2 \tag{1.2}$$

where $\rho(\mathbf{x})$ is the position dependent density of the resonator and $\mathbf{r}_n(x)$ is the normalized mode shape. As the amplitude of the mode is dependent on the position (x_0) this expression is even more complex, as it must be modified dividing by $|\mathbf{r}_n(x_0)|^2$, revealing that the position in the sample is important for the measurements.
Considering an oscillating force, the frequency dependent behaviour deriving from equation 1.1 is given by

$$x(\omega) = \chi(\omega)F(\omega) \tag{1.3}$$

where $\chi(\omega) = {}^1\!/_{m_{eff}\,(\Omega_m^2 - \omega^2) - i\Gamma_m m_{eff}\omega}$ is the mechanical susceptibility. The mechanical quality factor Q_m, a well known figure of merit for describing dissipation in mechanical resonators, is defined as:

$$Q_m = 2\pi\frac{\text{Energy stored per cycle}}{\text{Energy dissipated per cycle}} = \frac{m\Omega_m}{\Gamma_m} \tag{1.4}$$

1.2 Optical cavities

If two parallel mirrors are placed one in front of one another, light can reflect on their surfaces several times and can even remain confined in it. This is the idea of optical cavities, where a standing wave cavity resonator is formed. These cavities allow an optical beam to bounce back and forth. If the round-trip length (i.e., twice the cavity length, $2L$) is a multiple of the incident light wavelength (λ), the laser will constructively interfere

inside the cavity, amplifying the power inside it. This particular relation leads to a cavity optical frequency (ω_c) distribution following equation 1.5:

$$\omega_c = 2\pi\frac{c}{\lambda} = \frac{\pi c}{L}N \tag{1.5}$$

where c is the vacuum speed of light and N is an integer.
If we consider one individual cavity mode with frequency ω_o, the gain of the cavity when an incident flux of photons with a frequency ω_l is acting has the following behaviour [26,27]

$$\frac{da(t)}{dt} = i\Delta a(t) - \frac{\kappa}{2}a(t) + \sqrt{\kappa_\ell}\bar{a}_{in} \tag{1.6}$$

where $a(t)$ is the field inside the cavity, $\Delta = \omega_L - \omega_o$ is the detuning of the laser frequency ω_L with respect to the mode frequency ω_o, $\bar{a}_{in}$ is the incident optical field rate (meaning that $|\bar{a}_{in}|^2$ is the input photon rate), κ_ℓ is the loss rate into the side-coupled waveguide, and κ the total loss rate of the cavity.
From equation 1.6 the steady-state solution ($\frac{da(t)}{dt} = 0$) can be extracted for the field a and cavity population $|a|^2$, considering $P_L = \hbar\omega_l |\bar{a}_{in}|^2$ as the input laser power:

$$a = \frac{\sqrt{\kappa_\ell}a_{in}}{\frac{\kappa}{2} - i\Delta} \tag{1.7}$$

$$|a|^2 = \frac{\kappa_\ell}{\Delta^2 + (\kappa/2)^2}|a_{in}|^2 = \frac{\kappa_\ell}{\Delta^2 + (\kappa/2)^2}\frac{P_L}{\hbar\omega_l} \tag{1.8}$$

The experimental measurements of this work will be done through a bus-waveguide-coupled optical cavity coupling configuration, a schematic of which can be found in Figure 22. For this type of coupling $\kappa_\ell = \kappa_e/2$, being κ_e the external losses rate. Transmission and reflection expressions for this type of system can be expressed as follows [28]:

$$T(\Delta) = |t|^2 = \left|\frac{a_{\mathrm{out},t}}{a_{\mathrm{in}}}\right|^2 = \left|\frac{a_{\mathrm{in}} - \sqrt{\kappa_e/2}\,a}{a_{\mathrm{in}}}\right|^2 = \frac{\Delta^2 + (\kappa_i/2)^2}{\Delta^2 + (\kappa/2)^2} \tag{1.9}$$

$$R(\Delta) = |r|^2 = \left|\frac{a_{\mathrm{out},r}}{a_{\mathrm{in}}}\right|^2 = \left|\frac{-\sqrt{\kappa_e/2}\,a}{a_{\mathrm{in}}}\right|^2 = \frac{(\kappa_e/2)^2}{\Delta^2 + (\kappa/2)^2} \tag{1.10}$$

If $\kappa_e = 0, \mathrm{R} = 0$ and $\mathrm{T} = 1$ since the cavity is invisible to the bus waveguide and, as κ_e approaches κ, there will appear a dip centered at $\Delta = 0$ ($\omega_L = \omega_o$). For the minimum transmission point, $T(0) = (1 - \kappa_e/\kappa)^2$, this peak can reach $\mathrm{T} = 0$ when $\kappa_e = \kappa$.

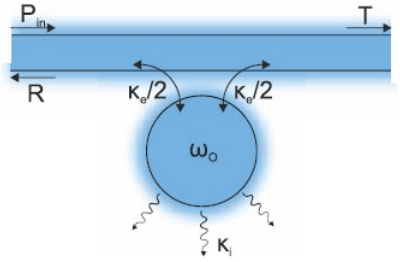

Figure 1: Schematic of a bus-waveguide-coupled optical cavity coupling configuration

As with mechanical resonators, the Q factor of the optical cavity can be calculated as

$$Q = \frac{\omega_o}{\kappa} \tag{1.11}$$

A detailed discussion of the concepts that will be used during this work including wave propagation in various periodic media, an introduction to photonic and phononic crystals, and Anderson localization (AL) can be found in **Appendix** C.

1.3 Radiation pressure

The behavior of how phonons propagate through different media can be understood by treating light as a wave (see **Appendix** C). Nevertheless, particle-wave duality and De Broglie's hypothesis [29] lead to the momentum p of the photon of wavelength λ

$$p = \hbar k \quad \left(\text{where} \quad k = \frac{2\pi}{\lambda}\right) \tag{1.12}$$

The reflection of a single photon off of a surface imparts a momentum transfer of $\Delta p = 2\hbar k$. If this photon comes from a coherent light beam with a photon rate $|\bar{a}_{in}|^2$, the beam would exert a force, known as the so-called radiation pressure force [30, 31], F_{RP}, given by:

$$F_{RP} = \frac{\Delta p}{\Delta t} = 2\hbar k \, |\bar{a}_{in}|^2 \tag{1.13}$$

Given the P_L definition, the force can be related to the laser power by

$$F_{RP} = \frac{2kP_L}{\omega_l} = \frac{2P_L}{c} \tag{1.14}$$

The momentum transfer from these photons to macroscopic mirrors is generally negligible. However, by creating an optical cavity using a second mirror as the illustrated in fig. 2, a resonant photon makes multiple round-trips before being lost either via leakage or absorption, increasing F_{RP} acting on the mirror surface [11].

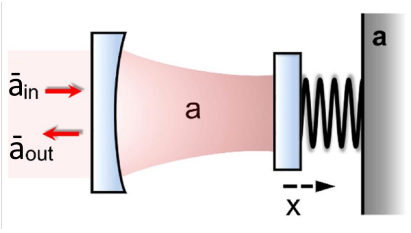

Figure 2: Schematic illustration of an optomechanical cavity

In such a cavity with a length L and corresponding frequency ω_o, if the circulating power P_{circ} is written in terms of the cavity photons $|a|^2$ and the round-trip time $\tau_{rt} = 2L/c$, the formula can also be expressed as

$$F_{RP} = \frac{2P_{\text{circ}}}{c} = \frac{2\hbar\omega_o}{c}\frac{|a|^2}{\tau_{rt}} = \frac{\hbar\omega_o|a|^2}{L} \equiv \hbar G|a|^2 \tag{1.15}$$

where $G \equiv \omega_o/L$ is the optomechanical coupling rate that can be interpreted as the frequency shift induced by a small mechanical displacement of the mirror and is related to the radiation-pressure force exerted by a single cavity photon. Generally, for optomechanical systems the vacuum optomechanical coupling rate g_o is preferred. This value corresponds to the frequency shift of the cavity due to a displacement equal to the zero-point fluctuations x_{zpf} and relates to G as

$$g_o = G x_{zpf} \tag{1.16}$$

$$\text{where } x_{zpf} = \sqrt{\hbar/2m_{eff}\Omega_m}$$

These types of optical cavity systems are used, for example, in gravitational wave detectors, such as LIGO, where the results are obtained precisely from displacement measurements. In this case, this radiation pressure is a hindrance which serves as a source of uncertainty in the displacement measurement [32, 33]. Nevertheless, for optomechanical (OM) purposes, the effect of this force is of relevant interest as it allows phonons to be introduced into a system.

1.4 Dynamics of optomechanical resonators

Assuming that the interaction occurs between a single pair of coupled optical and mechanical modes, the dynamics of such a system can be described by

$$\frac{da(t)}{dt} = i(\Delta + Gx(t))a(t) - \frac{\kappa}{2}a(t) + \sqrt{\kappa_\ell}\bar{a}_{in} \tag{1.17}$$

$$m_{eff}\frac{d^2x(t)}{dt^2} = -m_{eff}\Omega_m^2 x(t) - m_{eff}\Gamma_m\frac{d}{dt}x(t) + \hbar G|a(t)|^2 + F_{th} \tag{1.18}$$

where, $|\bar{a}_{in}|^2$ is the input photon flux, $\kappa = \kappa_e + \kappa_i$ is the sum of external and internal optical losses, $\Delta = \omega_L - \omega_0$ is the detuning of the pump laser frequency from the optical resonance frequency, and m_{eff}, Ω_m, and Γ_m, respectively represent the effective mass, resonance frequency, and decay rate of the mechanical resonator. Equation 1.18 is then 1.1 with $F(t) = F_{RP} + F_{th}$ i.e., radiation pressure force and a thermal excitation force. The output photon flux $|\bar{a}_{\text{out}}|^2$ is related to the input via

$$\bar{a}_{\text{out}}(t) = \bar{a}_{\text{in}} - \sqrt{\kappa_\ell}\bar{a}(t) \tag{1.19}$$

If equations 1.17 and 1.18 are studied for $G = 0$, we would have the equations for a coupled mode driven optical cavity and the dynamics of a thermally-driven damped harmonic oscillator. Their physics can be studied separately through the equations shown in sections 1.1 and 1.3. The system can be further simplified if neglecting the thermal force, as it is a low value stochastic excitation.

1.4.1 Optomechanical effects

In the scenario in which $G \neq 0$, the optical cavity and the mechanical resonator do not act independently. Introducing the cavity population $|\bar{a}|^2$ calculated from eq. 1.8, the radiation pressure force in the steady state is

$$F_{rp}(x) = \hbar G|\bar{a}|^2 = \frac{\hbar G\kappa_\ell}{(\kappa/2)^2 + (\Delta + Gx)^2}\,|\bar{a}_{in}|^2 \tag{1.20}$$

which is a conservative force that would change the bare harmonic potential of the mechanical resonator as

$$V(x) = V_{rp}(x) + \frac{1}{2}m_{eff}\Omega_m^2 x^2 \tag{1.21}$$

where the light-induced potential $V_{rp}(x)$ is

$$V_{rp}(x) = 2\hbar\frac{\kappa_\ell}{\kappa}\,|\bar{a}_{in}|^2 \arctan\left(\frac{2(\Delta + Gx)}{\kappa}\right) \tag{1.22}$$

This potential function is now dependent on the laser photon flux $\bar{a}_{in}$. The addition of $V_{rp}(x)$ changes the curvature at the minimum of the potential, thus changing the effective spring constant. The system can be still described as a damped mechanical resonator, but some of the parameters, like the mechanical frequency or the damping, will have deviations from the initial value.
Appendix B describes the dynamics the system undergoes in that situation. The conclusion leads to the following expression that shows the evolution of the damping Γ_{eff} in the case of a weak laser drive ($g_o \ll \kappa$), i.e., evaluating them at the unperturbed oscillation frequency $\omega = \Omega_m$.

$$\Gamma_{eff} = \Gamma_m + \Gamma_{om} = \Gamma_m + g_o^2|\bar{a}|^2 \left(\frac{\kappa}{\left(\bar{\Delta} + \Omega_m\right)^2 + (\kappa/2)^2} - \frac{\kappa}{\left(\bar{\Delta} - \Omega_m\right)^2 + (\kappa/2)^2} \right) \quad (1.23)$$

Here, a blue detuned laser ($\Delta > 0$) reduces the effective damping of the mechanical resonator as $\Gamma_{om}(\omega) \leq 0$. This effect can be observed experimentally (see section 2.4.1). By plotting the damping as a function of the incident laser power it is possible to calculate the value of g_o.

1.4.2 Dynamical backaction and lasing

When increasing the power, mechanical oscillations of the phononic mode grow exponentially up to a maximum amplitude. As gain starts to compensate losses, the reduction of the Γ_{eff} results in a narrowing in the mechanical peak. As seen in **Appendix** A, this growth can not extend infinitely due to damping in the system (thermoelastic damping, air damping, etc.), so it saturates at some maximum value.
Following the effective damping behaviour, there is a certain incident laser power P_{in} where $\Gamma_{eff} = 0$ i.e., $\Gamma_{om} = -\Gamma_m$. By introducing equation 1.8 in eq. 1.23, this power threshold results in

$$P_{th} = -\Gamma_m \frac{\hbar\omega_l}{g_o^2} \left(\frac{(\kappa/2)^2 + \bar{\Delta}^2}{\kappa_l} \right) \left(\frac{\kappa}{(\bar{\Delta} + \Omega_m)^2 + (\kappa/2)^2} - \frac{\kappa}{(\bar{\Delta} - \Omega_m)^2 + (\kappa/2)^2} \right)^{-1} \quad (1.24)$$

Whenever $P_{\text{in}} > P_{\text{th}}$ the intrinsic mechanical losses are compensated and high-amplitude coherent mechanical oscillations are activated. As in photonics, this regime in which the mechanical oscillations are self-sustained, almost monochromatic, and coherent is referred to as mechanical lasing.

2 Optomechanical platform

This section will present the optomechanical system under study. By storing light in a cavity it allows to improved light-matter interactions enabling phonon lasing in both the MHz and GHz regime by optically driving an Anderson-localized photonic mode.

2.1 Sample description

The samples consist of a 220 nm thick silicon (Si) Phononic Crystal (PnC) waveguide incorporating a periodic shamrock pattern (see Figure 3a). This PnC possesses a bandgap in the GHz range and has a line defect that creates a guided mode at 6.8 GHz [34]. The guided mode profile can be seen in Figure 3b and design details are given in [35].
At both ends, the PnC periodicity is changed (see Figure 3a). These regions with a different lattice constant act as acoustic shields for the waveguide as they have a larger lattice constant, resulting in a different band structure [35]. This change shifts the guided mode to a lower frequency and prevents coupling between the modes of each section. As the frequency of interest does not correspond to a mode in the shields, it is reflected when it arrives at the interface between the shield and the center waveguide, resulting in confinement of the mechanical mode.
Two of these PnC are placed with mirror y-symmetry creating, at the centre of the structure, a 45 nm wide air slot (see the SEM, Scanning Electron Microscope, image in Figure 4a). This design creates an optical cavity at the centre of each phononic crystal, i.e., we have both a photonic and phononic cavities within the same structure.
In addition to the guided mode, each PnC has its characteristic vibration modes. Figure 3c shows the profile for the in-plane breathing mode. As it is seen, compared to the guided mode, this mode extends through the structure and does not only propagate along the line defect. The coexistence of this modes in the same platform at different frequencies can allow to modulate the GHz mechanical displacements.

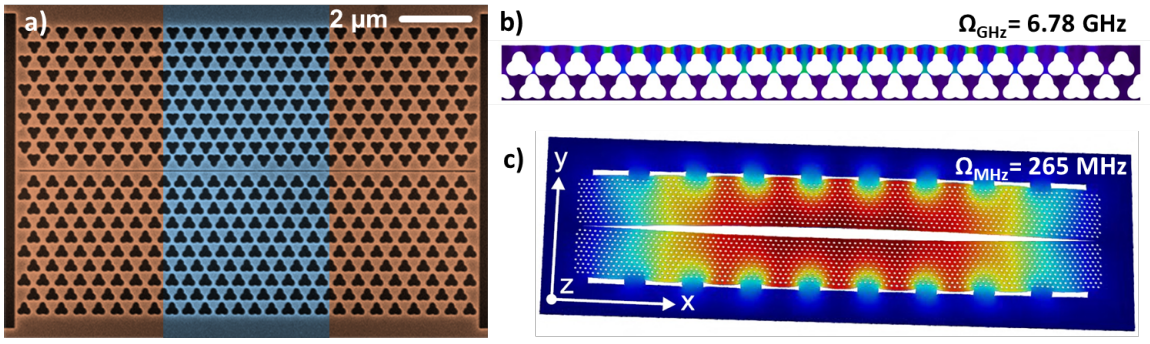

Figure 3: **a)** SEM image of the structure showing the air slot and the different PnCs for the center and shield regions in blue and brown, respectively. **b)** Mode profile for the guided mode (Reprinted figure with permission from Guilhem Madiot and Ryan C Ng (2022) Optomechanical generation of coherent GHz vibrations in a phononic waveguide [35]). **c)** Mode profile for the breathing mode of the structure.

Due to inherent nanofabrication imperfections the sidewalls of the slot offer some roughness that act as scattering points for the light inside it. Figure 4a shows a SEM image zooming at the air slot where the non-flat walls of the structure are visible. Anderson Localization (discussed in **Appendix** C) is also present in the structure as these scatterers can lead

to light interference and confinement. This posibility of high interactions between the optical field and the structure is of a great interest for the main objective of this design: OM coupling.

2.2 Optomechanical characterization setup

Near-field optical and optomechanical properties were examined by placing a tapered fiber loop in contact with the structure along the waveguide axis. Through that contact the fiber can evanescently couple with the optical cavity modes. This method is widely used in cavity optomechanics [36].
A mono-mode fiber taper is fabricated from a telecom optical fiber (SMF-28). After removing the coating of the fiber, it is heated at 1180^{o}C with a ceramic microheater while stretched by two micromanipulators [37]. To allow a more precise contact, a loop is created by twisting the fiber (2π rotation on each side: 4π total twist) and approaching its two endpoints. The desired size is obtained by pulling again and reducing the loop's dimension.
The optical fiber is connected to a high-power tunable laser (Yenista Tunics T100S-HP/SCL) that operates from 1440 to 1640nm. The output signal is then measured with a high speed photo-detector and split into a DC and an AC component (see schematic in figure 4c).

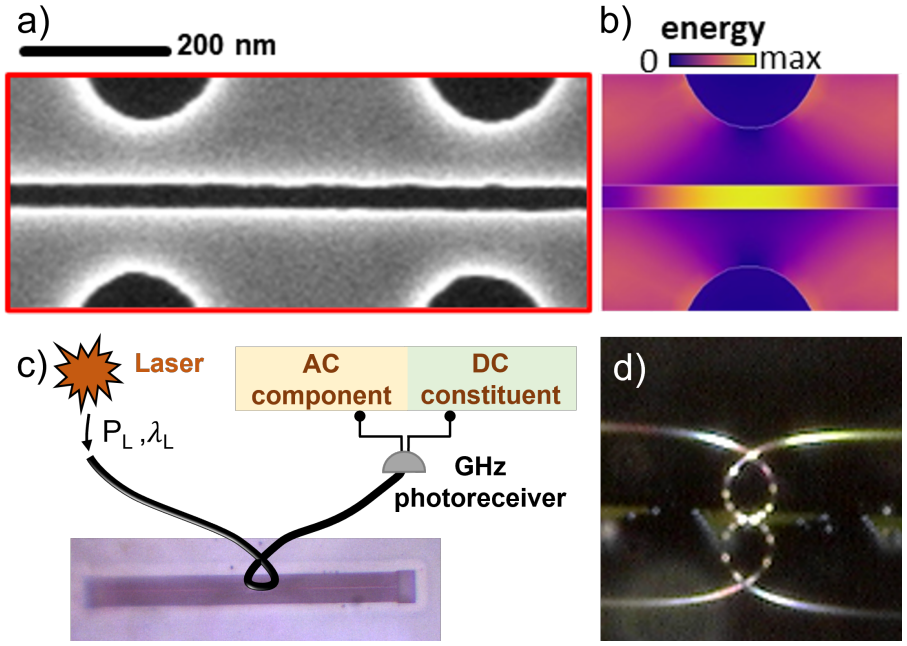

Figure 4: **a)** SEM image of the structure under study showing the air slot. **b)** Mode profile for the optical mode showing its confinement inside the slot (Madiot, Ng et al. (2022) Optomechanical generation of coherent GHz vibrations in a phononic waveguide [35]) **c)** OM setup schematic. d) Image of the loop in contact with the sample.

2.3 Optical characterization

By placing the tip of the taped fiber loop on the slot of the waveguide (Figure 4d), it is possible to evanescently couple into optical cavity modes such as the one shown in Figure

4b. A representative optical DC spectrum is shown in Figure 20a in **Appendix** E, in which resonant cavity optical modes manifest as transmission dips. The overlap of the evanescent fields of the two modes i.e., the fiber taper and the optical cavity one, enables their coupling whenever the two have the same frequency and are phase-matched (same k vector). The spectra shows both the Fabry-Pérot modes and the localized modes with no distinction. Madiot, Ng et al. [35] exhibits a similar figure with the average transmission spectra along the air slot where the Fabry-Pérot modes are differentiated from the localized modes.

2.3.1 Optical resonance characterization

At low power inputs, the cavity has low field values, meaning that the radiation pressure force is very small. For sufficiently small input powers, mechanics can be neglected and transition peaks follow equation 1.9.
Figure 5 shows a transmission peak measured for a low incident power measurement (<0.2mW). The peak is centered at $\omega_o = 2\pi \cdot 201.179$ THz and is the one used to transduce the mechanics of the system. By fitting the corresponding equation, the values of the different loss rates can be extracted. In this case, $\kappa_i = 2\pi \cdot 6.258$ GHz and $\kappa = 2\pi \cdot 8.390$ GHz. This means that $\kappa_e = 2\pi \cdot 2.132$ GHz. The quality factor Q of the peak can also be obtained from equation 1.10, giving a result of $Q = 23978$.

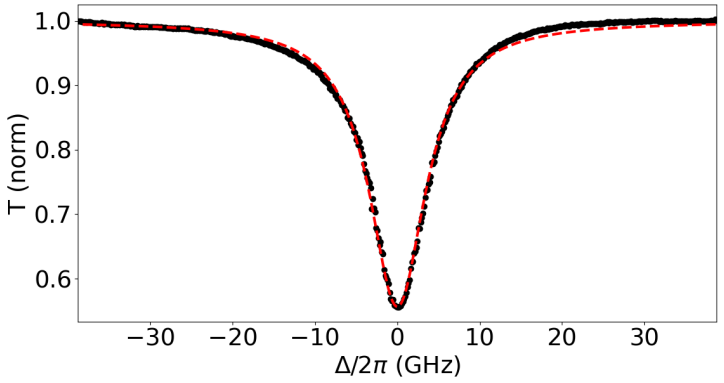

Figure 5: Experimental transmission peak: experimental data (black dots) are fitted by equation 1.9 (red line)

2.3.2 Thermo-optical effects and Self-Pulsing (SP)

Light interaction with the sample does not only limit to the mechanics, it can also affect the free carrier density and the temperature. The group index of a material changes with temperature due to the thermo-optic effect. This change, which can be considered linear for low temperatures ($< 600K$) is given by the thermo-optic coefficient, dn/dT. This behaviour causes non-linear dynamics when the laser power, P_L, is increased.
Other non-linear processes must be considered to fully describe a system. Effects such as free carrier absorption (FCA) and two-photon absorption (TPA) constantly occur in a structure, which consequently increase the temperature, especially through thermal relaxation. Due to the thermo-optic effect, the refractive index n will change, shifting the cavity's resonance frequency ω_o. The same occurs depending on the concentration of free carriers (N).

As Figure 20 shows, the group index of the system is a key factor that determines how Fabry-Pérot optical modes are distributed. Whenever this group index changes, the peaks will have a different resonance frequency. A simple description of how the mode's optical frequency ω_o' would change from its initial value ω_o depending on the carrier density (N) and the temperature increase (ΔT) can be

$$\omega_o' = \omega_o - \frac{\omega_o}{n_o}\frac{dn}{dN}N - \frac{\omega_o}{n_o}\frac{dn}{dT}\Delta T \tag{2.1}$$

where $\frac{dn}{dN}$ is the group index variation derived from the presence of free carriers, $\frac{dn}{dT}$ is the group index variation caused by temperature increase i.e., the first order thermo-optic coefficient, and n_o is the original group index. The consequence of such shifts in resonance frequency allow for the observation of bi-stabilities such the one shown in Figure 6. Two stable solutions are possible and can be reached depending on the detuning we approach the resonance with.
When coupling with the optical mode from a blue-shifted detuning (black line in Figure 6a), the field inside the cavity increases, causing the temperature to increase as well. This temperature increase causes the resonance frequency to red-shift, i.e. the resonance wavelength shifts to a higher one. If a wavelength sweep is done for the transmission measurement, a dip like the one shown in Figure 5 for low input powers would result in a similar spectra as the shown in black Figure 6a.
Nevertheless, when the optical mode is approached with a red-shifted frequency (red line in Figure 6a), the mode cannot be coupled until the detuning is sufficiently reduced. When that point is reached, the field can increase in the cavity and the depth in transmission is seen. This also causes the temperature to increase, so the optical resonance frequency is red-shifted again and the back and forth states coincide.

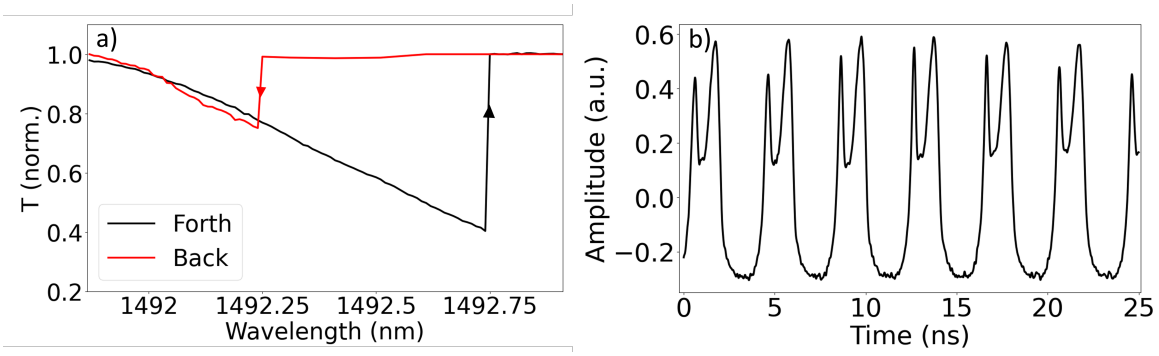

Figure 6: Right: Bi-stability experimental measure. Left: Experimental timetrace of Self Pulsing

Temperature and carrier density are two variables that depend on the number of photons inside a cavity. At the same time, changing those two parameters would change the "effective" frequency of the mode, increasing the detuning and consequently decreasing the field and the number of photons inside the cavity. This situation leads to a limit-cycle in which the coupling into the cavity, and thus the transmission, are being controlled by N and ΔT and change in time. This is known as Self-Pulsing (SP).
The Self-Pulsing regime results from the interplay between thermo-optic (TO) effects and free carrier dispersion (FCD) [38, 39]. These effects have a repercussion on the detuning but, more importantly, they have different response times. The fast characteristic response of free carriers due to light absorption followed by the slow reaction of the temperature,

mainly due to thermal relaxation of the carriers, causes behaviours like the one shown in Figure 6b extracted from the experimental system. The dynamic competition among these effects results in a strong an-harmonic modulation of the light in a stable regime. The signature temporal behaviour of SP is a quick increase in the transmission, due to the free carrier absorption, followed by another peak resulting from the subsequent thermalization. The characteristic Fast Fourier Transform (FFT) has the shape of multiple peaks spectrally located at integers of main SP frequency (ν_{SP}). Both mechanical lasing and SP can coexist in the same system, which can lead to a large variety of dynamical regimes such as synchronization [40] or chaos [41].

2.4 Optomechanical characterization methods

The output signal is divided into a DC and AC components, with the latter corresponding to the radio-frequency (RF) domain. This AC constituent can be studied in an electronic spectrum analyzer (ESA) allowing for the mechanical behavior of the system to be visualized (see **Appendix** D). The extent of the OM coupling is measured through the g_o parameter. Depending on this value, the different modes present in the structure would behave differently to the input laser. This constant can be obtained using different methods, two of which are explained in this section.

2.4.1 Calibration of g_o via optomechanical narrowing

From equation 1.23 in section 1.4.1 it was proven that, by increasing the input power (P_L), the linewidth of the mechanical peak narrows. This relation is plotted in Figure 7b for the guided mode (Ω_m= 6.8 GHz). For powers as low as 1.8 mW the peak is already lasing, as indicated by the effective damping value stabilization. At different positions along the waveguide and driving different localized modes the g_o value can change [35]
For the particular localized optical mode of interest, the effective damping, Γ_{eff}, starts to lower from $\Gamma_{eff} = \Gamma_m$ at approximately 0.4mW. The value of the damping when the mode is thermally activated, i.e. when backaction is still negligible, is the corresponding mechanical damping of the mode. The damping parameter has a value on the order of $\mathbf{\Gamma_m/2\pi = 5.15\ MHz}$. After that, the effective damping decreases until it saturates at $\Gamma_{eff} \approx 0$ at around 1.75mW. Through this linear decay in the damping of the mechanical mode, a value of $\mathbf{g_o/2\pi = 183.8\ kHz}$ can be extrapolated.

2.4.2 Calibration of g_o via phase modulation method

Moreover, an approximate value of the g_o parameter can also be extracted using a phase modulated signal [42]. This second method compares the power spectral density (PSD) of the known modulated signal and that of the mechanical mode. An approximate value of the parameter can be obtained through a single measurement via:

$$g_0^2 \approx \frac{1}{2\langle n_{\mathrm{m}}\rangle}\frac{\phi_0^2\Omega_{\mathrm{mod}}^2}{2}\frac{S_{II}^{\mathrm{meas}}(\Omega_{\mathrm{m}})\cdot\Gamma_{\mathrm{m}}/4}{S_{II}^{\mathrm{meas}}(\Omega_{\mathrm{mod}})\cdot\mathrm{ENBW}} \tag{2.2}$$

where ENBW is the effective noise bandwidth, Ω_{mod} is the modulated frequency, $\langle n_{\mathrm{m}}\rangle$ in the mechanical occupation number, and $S_{II}^{\mathrm{meas}}(\Omega_{\mathrm{mod}})$ correspond to the PDS of the mechanical and modulated frequency peaks, respectively.
This approximation becomes more valid for large mechanical occupation numbers $\langle n_{\mathrm{m}}\rangle \approx k_{\mathrm{B}}T/\hbar\Omega_{\mathrm{m}} \gg 1$. Using this method, a result for the vacuum optomechanical coupling rate of similar order of magnitude is obtained for the GHz guided mode.

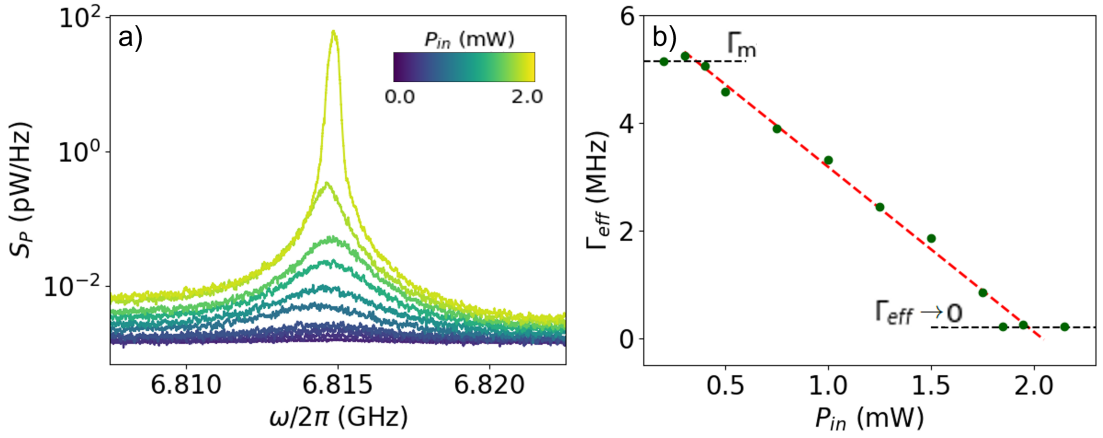

Figure 7: **a)** Radio-frequency spectrum showing the mechanical mode for different input laser powers. Dynamical back-action is observed, which leads to mechanical lasing. **b)** Corresponding effective mechanical damping as a function of the power. Three regimes are seen: thermal ($\Gamma_{eff} = \Gamma_m$), dynamical backaction (in red), and mechanical lasing ($\Gamma_{eff} \rightarrow 0$)

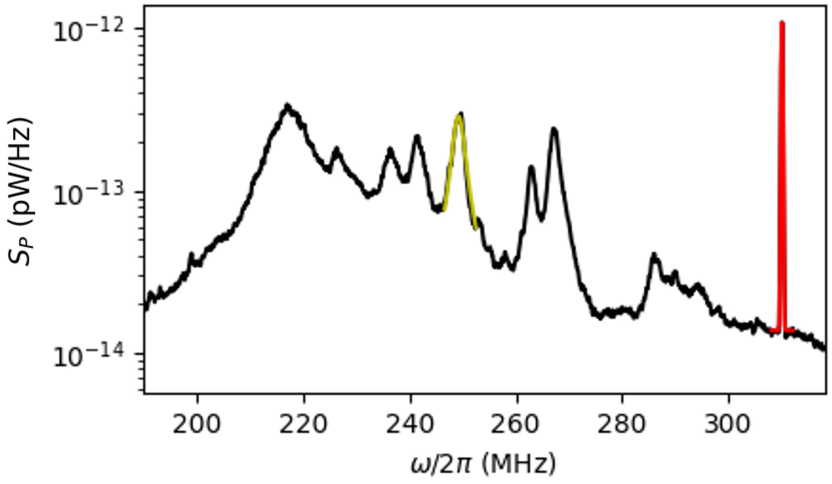

Figure 8: Spectral measurement for the $g_{o_{MHz}}$ showing the mechanical peak in the thermal regime and the modulated signal at 310 MHz

Apart from the GHz guided mode, the spectra shows that a mode around 265 MHz also begins to lase for higher input powers (P_L). This mode corresponds to the characteristic breathing in-plane mode of the platform shown in Figure 3c. Through this method, the corresponding g_o value for this mode can also be attained (see Figure 8). In this case, the value corresponds to $\mathbf{g_o/2\pi = 77.89\ kHz}$.
The mechanical damping of this MHz mode can be extracted from a low input power measurement of the mechanical spectra. By fitting the curve when the mode is still being thermally activated. The result leads to a $\mathbf{\Gamma_m/2\pi = 2.81\ MHz}$
This considerable difference in the coupling with this mode compared with the guided one leads to a particular situation. As the field inside the cavity is increased, the two regimes start to be thermally activated. Gradually, the GHz peak begins to narrow and increase in

intensity until it lases. Meanwhile, the MHz mode continues to be in the thermal regime until reaching its particular P_{th}, where both modes can lase at the same time.
Table 1 includes a compilation of the most important values of the sample and the setup extracted until now.

Parameter	Value	Description
ω_o	2π·201.179 THz	Optical mode frequency
κ_i	2π·6.258 GHz	Internal optical losses
κ_e	2π·2.132 GHz	External optical losses
κ	2π·8.390 GHz	Total optical losses
Γ_{MHz}	2π·2.81 MHz	Damping MHz peak
Γ_{GHz}	2π·5.15 MHz	Damping GHz peak
Ω_{MHz}	2π·265 MHz	MHz peak mechanical frequency
Ω_{GHz}	2π·6.78 GHz	GHz peak mechanical frequency
$g_{o_{MHz}}$	2π·77.89 kHz	MHz peak vacuum optomechanical coupling rate
$g_{o_{GHz}}$	2π·183.8 kHz	GHz peak vacuum optomechanical coupling rate

Table 1: Sample OM parameters

3 M-O-M GHz mechanical frequency comb

Driving an Anderson localized optical mode will allow optomechanical interactions with different couplings to the mechanics. One of those localized modes is found around λ= 1490.2 nm ($\omega_0 = 2\pi$·201.179 THz) and previous measurements show that it can be driven to couple to the mechanical modes of the platform. Through this optical mode, OM coupling is achieved and is used to stimulate mechanics both in the MHz and the GHz simultaneously. The emergence of a regime of a mechanical comb formation is observed, giving rise to a periodic spectral feature centered at 6.7 GHz with a width of around 2 GHz.

3.1 Theoretical model

The potential of the system to drive two mechanical modes with a single optical localized mode can be modeled with a set of equations similar to the ones shown in section 1.4. In this case, the fact that there exists two mechanical modes of frequencies Ω_{MHz} and Ω_{GHz} coupled with different optomechanical coupling rates to the optical mode would have to be taken into account. A schematic of the interaction between a driven optical mode and two mechanical resonators including the main parameters is shown in Figure 22.
An assumption is done considering the two vibrating modes as two different independent mechanical resonators coupled through the driven optical mode and no direct coupling between the two mechanical equations is taken into account. Neglecting the thermo-optic effect of increasing the incident power, the set of equations which can describe the characteristics of the system is:

$$\dot{a} = i(\Delta + G_{_{MHz}}x_1 + G_{_{GHz}}x_2)a - \frac{\kappa}{2}a + \sqrt{\kappa_e/2}a_{in}$$

$$\ddot{x_1} = -\Gamma_{MHz}\dot{x_1} - \Omega^2_{MHz}x_1 + \frac{\hbar G_{MHz}}{m_{eff_{GHz}}}|a|^2 \tag{3.3}$$
$$\ddot{x_2} = -\Gamma_{GHz}\dot{x_2} - \Omega^2_{GHz}x_2 + \frac{\hbar G_{GHz}}{m_{eff_{GHz}}}|a|^2$$

where G_{MHz}, Γ_{MHz} and, $m_{eff_{MHz}}$ are the MHz mode optomechanical coupling rate, mechanical damping factor and, effective mass, respectivelly. G_{GHz}, Γ_{GHz} and, $m_{eff_{GHz}}$ are the analogous parameters for the GHz mode.
The formula for the effective mass of a certain mode of a resonator is shown in equation 1.2 highlighting the importance of the position along the waveguide for the measurements. The m_{eff} can also be calculated from finite elements method (FEM) simulations, but the use of this parameter can be avoided by renormalizing the above equations 3.3 using the variable $\mathbf{x}_i = \frac{x_n}{x_{zpf,n}c}$ and the vacuum optomechanical coupling rate $g_{o_n} = G_n x_{zpf,n}$. The zero point fluctuation displacement, $x_{zpf,n}$, of the mechanical resonator can be calculated with the expression given in equation 1.16. By doing so, the set of equations ends up as:

$$\dot{a} = i(\Delta + g_{o_{MHz}}\mathbf{x}_1 + g_{o_{GHz}}\mathbf{x}_2)a - \frac{\kappa}{2}a + \sqrt{\kappa_e/2}a_{in}$$
$$\ddot{\mathbf{x}_1} = -\Gamma_{MHz}\dot{\mathbf{x}_1} - \Omega^2_{MHz}\mathbf{x}_1 + 2\Omega_{MHz}g_{o_{MHz}}|a|^2 \tag{3.4}$$
$$\ddot{\mathbf{x}_2} = -\Gamma_{GHz}\dot{\mathbf{x}_2} - \Omega^2_{GHz}\mathbf{x}_2 + 2\Omega_{GHz}g_{o_{GHz}}|a|^2$$

The set of equations 3.4 involves now multiple parameters that can be evaluated experimentally from different measurements. The ensemble of the parameters and values, that have been discussed during the development of this work, is presented in Table 1. The optical parameters such as ω_o, κ_i, κ_e, and κ were extracted from the low power (<0.2mW) transmission measurement of the peak shown in Figure 5. Mechanical and optomechanical parameters calculation, like Γ_n, Ω_n and g_{o_n}, is discussed in Section 2.4 and their corresponding values are summarized in Table 1 as well. In this way, the field excites each mode through the vacuum coupling rate and, in consequence, it also changes when the mechanics start to emerge.
The output signal, that is directly related to the transmission (T), can be extracted from equation 1.19 for a given input laser power $P_L = \hbar\omega_l |\bar{a}_{in}|^2$. This set of equation allow for a qualitative prediction of the behavior of the system when driving it at different optical frequencies around the resonance (ω_o). By computing the time trace of the transmission and its corresponding FFT, a comparison with the experimental data can be done.

3.2 Mechanical comb formation

Experimentally, when increasing the input power, thermo-optic effects become more apparent and the optical transmission dip begins to experience a red shift (see section 2.3.2). This means that in order to reduce the detuning of the laser, the optics will be driven with a different, lower, optical frequency than the initial resonance to start to excite the mechanics.
The DC constituent of the transmission is used to check when the optical mode is being driven looking at the transmission dip. The optical mode of interest that has its resonance frequency at $\omega_o = 2\pi{\cdot}201.179$ THz, corresponding to a wavelength of $\lambda = 1490.2$ nm, can experience a shift as high as 4.5 nm in wavelength when $P_L = 6.5$ mW (see Figure 9a).
This P_L was chosen deliberately as it is greater than the corresponding P_{th} of each of the mechanical modes under study. Exciting the mechanics with that optical mode at such incident laser powers allows both modes to lase at the same time. Figure 9 shows all

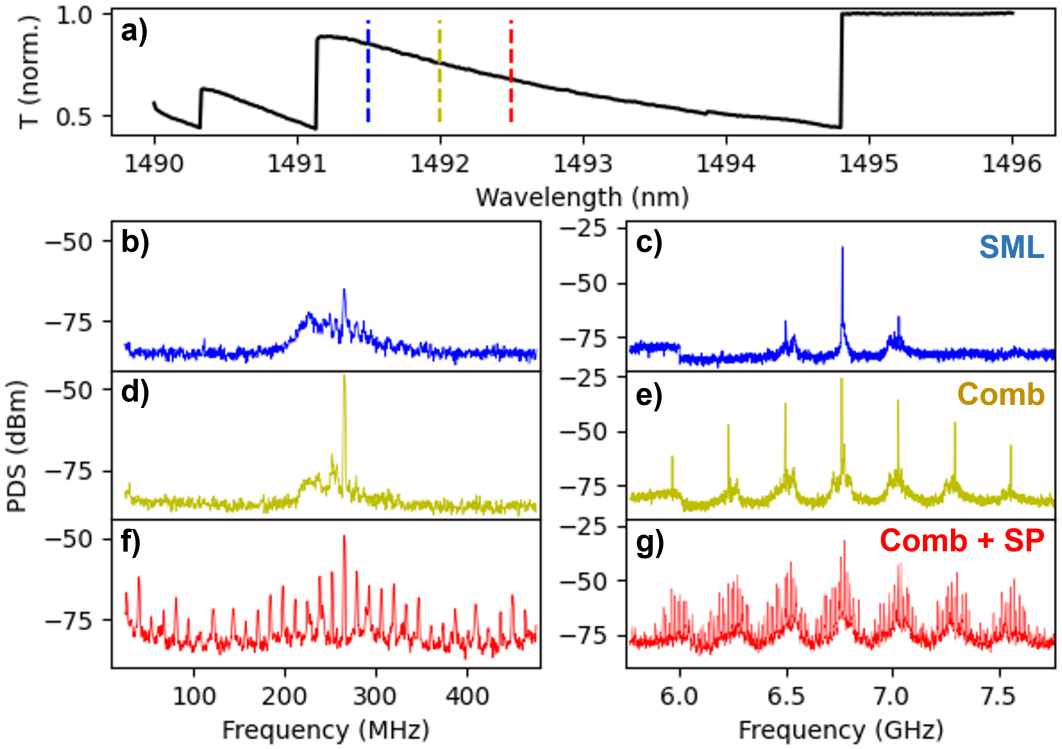

Figure 9: Different regimes of the system when driven at P_L=6.5mW showing the MHz and GHz spectra. a) Optical transmission peak. b and c) Single mode lasing (SML). d and e) Comb formation f and g) Comb formation and Self-Pulsing

the salient features of the mechanics when driving the optical mode under study from a blue-shifted detuning.

Transmission depth can serve as an indirect indicator of the radiation pressure force that the system undergoes. As we saw in Section 1.3, the exerted force is proportional to the field inside the cavity. Having a dip in the transmission is directly related to an increase of the field inside the cavity, meaning that there is a rise in the number of photons in the cavity as well.

Then, when we increase the field in the cavity, in this case by approaching the resonance with a red-shifted effective detuning, the mechanical motion will consequently be amplified due to dynamical backaction. The mode with a higher coupling rate, that in this case happens to be the Ω_{GHz} one, will be the first to lase at a higher detuning from the shifted resonance. Different behaviours can be studied in the structure.

The situation when the detuning is still high and only the guided mode at Ω_{GHz} is lasing is referred as SML, for Single Mode Lasing (see Figure 9c). Its spectrum shows a really intense peak in the mechanical frequency as studied in the g_o calibration Figure 7. Nevertheless, mechanics in the MHz regime are not inappreciable, as they are thermally excited as well (see Figure 9b). This also has an effect in the higher frequencies, as two side-bands are formed on each side of the lasing guided mode. This last observation will be of important relevance: in a manner akin to a modulator signal, the low frequency regime seems to modulate the GHz oscillations.

When the red-shifted effective detuning is further reduced, the regime where both 265 MHz and 6.8 GHz peaks are lasing is reached. Here, the amplitude of the Ω_{GHz} frequency

oscillations will start to be modulated with a frequency of Ω_{MHz} as both modes oscillations are self-sustained. Figure 9d shows the Ω_{MHz} mode lasing as the peak has considerably increased and narrowed. As the MHz peak is lasing, the mechanical spectra will not only exhibit the main peak at Ω_{MHz}, but the different harmonics at $M\Omega_{MHz}$ (being M an integer number) will also appear. This harmonics of the breathing in-plane mode are not visible in Figure 9, but can be seen if the span is increased. Figure 21 presents the full span of the ESA arriving to almost 14 GHz. The presence of this harmonics is translated into the emergance of their corresponding peaks in the sidebands of the Ω_{GHz} mode (see Figure 9e). A comb is formed around the guided mode frequency with a spectral separation corresponding to Ω_{MHz} and a width of 2 GHz. This feature gives the name to this regime in the Figure: Comb.

3.3 Theoretical vs experimental results

To clarify the origin of this behavior, the optomechanical model introduced in 3.3 is adapted including radiation pressure of the single localized mode driving the mechanics both in the MHz and in the GHz. At the end, the model results in three coupled second order differential equations: one for the optical cavity and the other two to describe each mechanical mode.
The model satisfactorily reproduces the experimental spectral response and the main features: the onset of lasing in the guided mode (Ω_{GHz}), followed by the formation of the frequency comb when the breathing mode (Ω_{MHz}) begins to lase (see Figure 10a and b). When the detuning from the optical mode is reduced, a peak in the GHz frequency starts to appear as it happened experimentally. After the peak narrowing and increase in amplitude in the GHz corresponding to the SML regime, the detuning is further reduced and mechanics in the MHz start to become visible. When performing the simulation at the optical frequency, the comb formation was also observed.
The time traces of each of the two regimes can be acquired experimentally using an oscilloscope (Tektronix MSO/DPO70000 Series) to plot the AC component of the transmission. Experimental time response of the transmission corresponding to the lasing regimes of the Ω_{GHz} mode and comb formation in the GHz are shown in Figures 10e and f, respectively. The first of these two shows an almost sinusoidal-shaped oscillation each 0.15 ns corresponding to the Ω_{GHz} frequency oscillations. The second one still shows the oscillations of the guided mode, but this time displaying a marked modulation of the envelope at 4 nm, i.e. the Ω_{MHz} frequency is modulating the previous one. Looking closely at Figure 10e, it can be seen that the amplitude of the oscillations is not constant with time and seems to be slightly modulated with a similar envelope at around Ω_{MHz}. This can be explained when taking into account the thermal activation of the breathing in-plane mode discussed in the previous section.
From the results of model, time traces can also be extracted and compared to the experimental data. Figure 10c shows the time dependence of the transmission for the regime where only the GHz mode lases and Figure 10d shows the time trace for the comb formation. The computed transmission closely follows the experimental behavior of the system at the two signature regimes. Even so, the Comb regime time trace seems to double the modulation frequency. This characteristic can be explained when looking at the FFT of the model in Figure 21 showing the second harmonic at $2\Omega_{MHz}$ with higher amplitude than the first harmonic at Ω_{MHz}. This can be explained as the saturation of the mechanics in the experimental platform due to non-linear elasticity of the mechanic resonator like the Duffing non-linear term, changing the potential with a higher order anharmonical term.

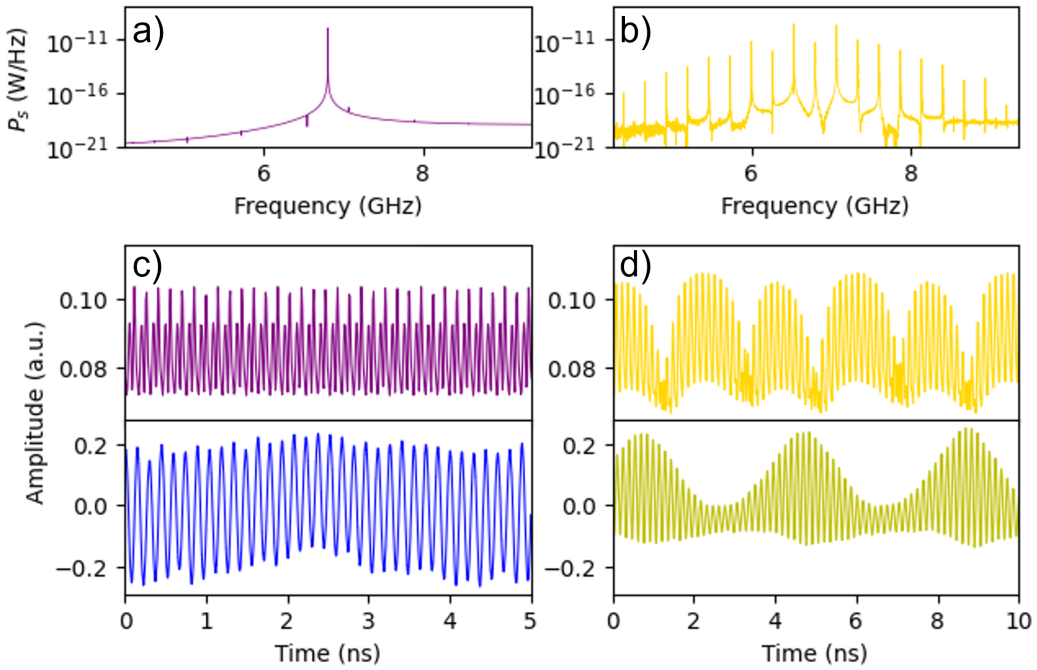

Figure 10: Model FFT for the SML (a) and Comb (b) regimes. c) Time traces of the transmission for SML for the model (Top) and experimental setup (Bottom). d) Time traces of the transmission for the Comb regime for the model (Top) and experimental setup (Bottom)

These non-lineraities are not considered in the simulations and so numerical saturation gains importance.

3.4 Non-linear effects: Self-Pulsing

To have a complete description of the system we would have to add several nonlinearities coming from temperature and free carriers. If phenomena such as free carrier absorption (FCA) and two-photon absorption (TPA) are considered, the generation of heat and free carriers would affect the results. The impact of an increase in temperature is seen experimentally in the transmission spectra shown in Figure 9a, blue-shifting the resonance frequency through the thermo-optic effect.
As explained in Section 2.3.2, the fast and slow characteristic response of carriers and temperature, respectively, will generate RF dynamics leading to Self-Pulsing (SP) limiting cycle and represent the last signature regime of the system: Comb + SP.
When the cavity field is sufficiently high, i.e. driving the optical mode with an even lower detuning, SP can also be achieved. Mechanical lasing and SP can simultaneously happen in the same system, so the new behaviour difference with the previous one in the frequency spectrum is the ofset of the SP peak. Figure 9f and 9g show the experimental data in this situation. The figure shows that, in the MHz regime, around the 265 MHz lasing peak a new comb is formed with peaks having a difference of about ω_{SP}=13.5 MHz. As occured when the Ω_{MHz} peak began to lase, the different harmonics were also present and arose in the GHz sidebands (Figure 9e). Now, the SP peak located at 13.5MHz and its harmonics are contributing to the comb formation in the MHz. Not only that, this spectra and its

corresponding harmonics also emerged in the principal comb's sidebands around Ω_{GHz}. As a result, we have a multiple comb formation. A main comb formed around Ω_{GHz} with a peak separation of Ω_{MHz}, where each of the peaks of the comb, including the central one, also exhibit a comb with a smaller spectral separation of ω_{SP} (see Figure 9f). A map showing when the different regimes emerge at each incident power is given in Figure 23 in **Appendix** F.
This last behaviour can also be modelled and other works include this effects in their models [21]. The incorporation of SP into the model will force the system to be described by at least two more differential equations: one for the density of free carriers (N) in the system and another for the temperature increase (ΔT).

4 Conclusion

A Mechanical-Optical-Mechanical (M-O-M) coupling is achieved in a Phononic Crystal (PnC) waveguide where a single Anderson Localized (AL) optical mode is able to excite the mechanics in the platform at frequencies with an order of magnitude of difference. The difference on the coupling rates of each of the excited modes induces the formation of a frequency comb centered at a mechanical carrier frequency of 6.8 GHz with a span on the order of 2 GHz when certain threshold power is surpassed. The experimental dynamics follow the predictions of the above presented three coupled equation model that only relies on the experimental characterization of the system's parameters. Frequency domain study has shown that the dynamics that the system undergoes when the comb is formed could extend to the tens of THz and experimental data seems to be in accordance with this data. Moreover, when non-linear effects like photon absorption by the carriers and temperature increase cease to be negligible, the experimental platform can experience Self-Pulsing, leading to an even more important modulation of the system's behaviour.
To our knowledge, this platform is is the first to show a self sustained frequency comb coming from purely from the mechanical dynamics of two vibration modes. The interplay of phonons and photons in this same structure including signal modulation is of a great interest for the development of phononic circuits [43] as well for optical signal processing. Other potential perspectives lead to synchronization and mechanical mode locking [44] and for metrological applications.

References

[1] *De Cometis Libelli Tres*. Johannes Kepler, Germany, 1619.

[2] Theodor W Hänsch and Arthur L Schawlow. *Optics Communications*, 13(1):68–69, 1975.

[3] Stig Stenholm. *Reviews of modern physics*, 58(3):699, 1986.

[4] Pierre-François Cohadon, Antoine Heidmann, and Michel Pinard. *Physical Review Letters*, 83(16):3174, 1999.

[5] Dustin Kleckner and Dirk Bouwmeester. *Nature*, 444(7115):75–78, 2006.

[6] M Poggio, CL Degen, HJ Mamin, and D Rugar. *Physical Review Letters*, 99(1):017201, 2007.

[7] Albert Schliesser, Pascal Del'Haye, Nima Nooshi, KJ Vahala, and Tobias J Kippenberg. *Physical Review Letters*, 97(24):243905, 2006.

[8] Jasper Chan, TP Alegre, Amir H Safavi-Naeini, Jeff T Hill, Alex Krause, Simon Gröblacher, Markus Aspelmeyer, and Oskar Painter. *Nature*, 478(7367):89–92, 2011.

[9] TJ Kippenberg, H Rokhsari, T Carmon, Axel Scherer, and KJ Vahala. *Physical Review Letters*, 95(3):033901, 2005.

[10] Markus Aspelmeyer, Tobias J. Kippenberg, and Florian Marquardt. *Rev. Mod. Phys.*, 86:1391–1452, Dec 2014.

[11] VB Braginski and AB Manukin. *Sov. Phys. JETP*, 25(4):653–655, 1967.

[12] Lei Wang and Baowen Li. *Physical review letters*, 99(17):177208, 2007.

[13] Nianbei Li, Jie Ren, Lei Wang, Gang Zhang, Peter Hänggi, and Baowen Li. *Reviews of Modern Physics*, 84(3):1045, 2012.

[14] Daiki Hatanaka, Imran Mahboob, Koji Onomitsu, and Hiroshi Yamaguchi. *Nature nanotechnology*, 9(7):520–524, 2014.

[15] Wei Fu, Zhen Shen, Yuntao Xu, Chang-Ling Zou, Risheng Cheng, Xu Han, and Hong X Tang. *Nature communications*, 10(1):1–7, 2019.

[16] Pascal Del'Haye, Albert Schliesser, Olivier Arcizet, Tom Wilken, Ronald Holzwarth, and Tobias J Kippenberg. *Nature*, 450(7173):1214–1217, 2007.

[17] Lin Chang, Songtao Liu, and John E Bowers. *Nature Photonics*, 16(2):95–108, 2022.

[18] Pascal Del'Haye, Olivier Arcizet, Michael L Gorodetsky, Ronald Holzwarth, and Tobias J Kippenberg. *Nature Photonics*, 3(9):529–533, 2009.

[19] Scott A Diddams, Leo Hollberg, and Vela Mbele. *Nature*, 445(7128):627–630, 2007.

[20] Zhi Jiang, Chen-Bin Huang, Daniel E Leaird, and Andrew M Weiner. *nature photonics*, 1(8):463–467, 2007.

[21] Pierre Etienne Allain, Biswarup Guha, Christophe Baker, David Parrain, Aristide Lemaître, Giuseppe Leo, and Ivan Favero. *Phys. Rev. Lett.*, 126:243901, Jun 2021.

[22] Adarsh Ganesan, Cuong Do, and Ashwin Seshia. *Physical review letters*, 118(3):033903, 2017.

[23] David A Czaplewski, Changyao Chen, Daniel Lopez, Oriel Shoshani, Axel M Eriksson, Scott Strachan, and Steven W Shaw. *Physical review letters*, 121(24):244302, 2018.

[24] Jing Zhang, Bo Peng, Seunghwi Kim, Faraz Monifi, Xuefeng Jiang, Yihang Li, Peng Yu, Lianqing Liu, Yu-xi Liu, Andrea Alù, et al. *Nature*, 600(7887):75–80, 2021.

[25] BD Hauer, C Doolin, KSD Beach, and JP Davis. *Annals of Physics*, 339:181–207, 2013.

[26] Qiang Li, Tao Wang, Yikai Su, Min Yan, and Min Qiu. *Optics express*, 18(8):8367–8382, 2010.

[27] Yoshihiro Akahane, Takashi Asano, Bong-Shik Song, and Susumu Noda. *Optics Express*, 13(4):1202–1214, 2005.

[28] Guillermo Arregui. *Light-motion interaction in disordered nanostructures*. PhD thesis, 2021.

[29] Louis de Broglie. *The London, Edinburgh, and Dublin Philosophical Magazine and Journal of Science*, 47(278):446–458, 1924.

[30] JH Poynting. *The London, Edinburgh, and Dublin Philosophical Magazine and Journal of Science*, 9(52):393–406, 1905.

[31] Tomaž Požar and Janez Možina. *Physical review letters*, 111(18):185501, 2013.

[32] Benjamin P Abbott, Richard Abbott, TD Abbott, MR Abernathy, Fausto Acernese, Kendall Ackley, Carl Adams, Thomas Adams, Paolo Addesso, RX Adhikari, et al. *Physical review letters*, 116(6):061102, 2016.

[33] BP Abbott, R Abbott, R Adhikari, P Ajith, Bruce Allen, G Allen, RS Amin, SB Anderson, WG Anderson, MA Arain, et al. *Reports on Progress in Physics*, 72(7):076901, 2009.

[34] Omar Florez, Guillermo Arregui, Marcus Albrechtsen, RC Ng, Jordi Gomis-Bresco, Søren Stobbe, CM Sotomayor-Torres, and Pedro David García. *arXiv preprint arXiv:2202.02166*, 2022.

[35] Guilhem Madiot, Ryan C Ng, Guillermo Arregui, Omar Florez, Marcus Albrechtsen, Søren Stobbe, Pedro D Garcia, and Clivia M Sotomayor-Torres. *arXiv preprint arXiv:2206.06913*, 2022.

[36] Chris P Michael, Matthew Borselli, Thomas J Johnson, C Chrystal, and Oskar Painter. *Optics express*, 15(8):4745–4752, 2007.

[37] Lu Ding, Cherif Belacel, Sara Ducci, Giuseppe Leo, and Ivan Favero. *Applied optics*, 49(13):2441–2445, 2010.

[38] D Navarro-Urrios, NE Capuj, J Gomis-Bresco, MF Colombano, PD García, M Sledzinska, F Alzina, A Griol, A Martinez, and CM Sotomayor-Torres. In *2016 18th International Conference on Transparent Optical Networks (ICTON)*, pages 1–4. IEEE, 2016.

[39] Thomas J Johnson, Matthew Borselli, and Oskar Painter. *Optics express*, 14(2):817–831, 2006.

[40] Martin F Colombano, Guillermo Arregui, Nestor E Capuj, A Pitanti, Jeremie Maire, Amadeu Griol, Blas Garrido, Alejandro Martínez, Clivia M Sotomayor-Torres, and Daniel Navarro-Urrios. *Physical review letters*, 123(1):017402, 2019.

[41] Jeremie Maire, Guillermo Arregui, Nestor E Capuj, Martin F Colombano, Amadeu Griol, Alejandro Martinez, Clivia M Sotomayor-Torres, and Daniel Navarro-Urrios. *APL Photonics*, 3(12):126102, 2018.

[42] ML Gorodetksy, Albert Schliesser, Georg Anetsberger, Samuel Deleglise, and Tobias J Kippenberg. *Optics express*, 18(22):23236–23246, 2010.

[43] Amir H. Safavi-Naeini, Dries Van Thourhout, Roel Baets, and Raphaël Van Laer. *Optica*, 6(2):213–232, Feb 2019.

[44] Georg Heinrich, Max Ludwig, Jiang Qian, Björn Kubala, and Florian Marquardt. *Phys. Rev. Lett.*, 107:043603, Jul 2011.

[45] James R Chelikowsky and Marvin L Cohen. *Physical Review B*, 14(2):556, 1976.

[46] James C Maxwell. *The London, Edinburgh, and Dublin Philosophical Magazine and Journal of Science*, 21(141):338–348, 1861.

[47] Michael Faraday. *Philosophical transactions of the Royal Society of London*, (121):299–340, 1831.

[48] Emil Lenz. *Annalen der Physik*, 107(31):483–494, 1834.

[49] James Clerk Maxwell. *Philosophical transactions of the Royal Society of London*, (155):459–512, 1865.

[50] Bartosz Janaszek and Paweł Szczepański. *Materials*, 14(15):4065, 2021.

[51] Ertugrul Cubukcu, Koray Aydin, Ekmel Ozbay, Stavroula Foteinopoulou, and Costas M Soukoulis. *Physical review letters*, 91(20):207401, 2003.

[52] Hideo Kosaka, Takayuki Kawashima, Akihisa Tomita, Masaya Notomi, Toshiaki Tamamura, Takashi Sato, and Shojiro Kawakami. *Applied Physics Letters*, 74(10):1370–1372, 1999.

[53] Alongkarn Chutinan, Nazir P Kherani, and Stefan Zukotynski. *Optics Express*, 17(11):8871–8878, 2009.

[54] Philip W Anderson. *Physical review*, 109(5):1492, 1958.

[55] Thomas Vasileiadis, Jeena Varghese, Visnja Babacic, Jordi Gomis-Bresco, Daniel Navarro Urrios, and Bartlomiej Graczykowski. *Journal of Applied Physics*, 129(16):160901, 2021.

VARIABLE COMPILATION LIST

Parameter	Description
m_{eff}	Effective mass
Γ_m	Decay rate of the mechanical oscillator
Ω_m	Mechanical frequency
ω_o	Cavity optical frequency
G	Optomechanical coupling rate
g_o	Vacuum optomechanical coupling rate
x_{zpf}	Zero point fluctuation
F_{RP}	Radiation pressure force
P_L	Incident laser power
ω_L	Laser optical frequency
$\Delta = \omega_L - \omega_o$	Detuning of the pump laser frequency from the optical resonance frequency
$\lvert\bar{a}_{in}\rvert$	Incident photon rate
κ_ℓ	Laser drive channel losses rate
κ_i	Internal optical losses rate
κ_e	External optical losses rate
κ	Total optical losses rate
n	Group index

Table 2: Optomechanic parameters

5 APPENDIX

A Mechanical oscillators basics

A.1 Harmonic oscillator

In classical mechanics, an harmonic oscillator is a system that, when displaced from its equilibrium position, experiences a restoring force F proportional to the displacement y:

$$\vec{F} = -k\vec{y} \tag{A.1}$$

where k is a positive constant. A typical harmonic oscillator is a mass attached to a spring (Figure 11), and the proportionality constant, k, between the force and the displacement is the spring constant. In that sense, when the system is displaced from its equilibrium position, it will experience a force that brings it back to it.

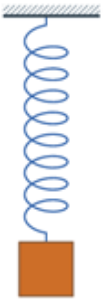

Figure 11: Spring-mass model

By simply applying the second Newton's law, we can see that:

$$m\frac{d^2y}{dt^2} = -ky \tag{A.2}$$

Solving the differential equation, we get:

$$y(t) = Ae^{i(\omega_0 t+\varphi)} \tag{A.3}$$

Where A is the amplitude of the movement, y is the position (being y=0 the equilibrium position) and φ is the initial phase for t=0. This movement corresponds to an oscillation at a characteristic angular frequency, called resonance frequency, of $\omega_0 = \sqrt{\frac{k}{m}}$. The relation of the angular frequency and the frequency is just $\omega_0 = 2\pi f$.

A.2 Damped harmonic oscilator

In real systems there are other forces that can affect the behaviour of the oscillator, such as friction. This type of forces act in the direction that is opposite to the movement and tend to attenuate the amplitude of the movement. They are called damping forces, and so the proportionality factor between it and the velocity (b in equation A.4), is the viscous damping coefficient.

$$m\frac{d^2y}{dt^2} = -ky - b\frac{dy}{dt} \tag{A.4}$$

From the second Newton's law, what we obtain is now that the position with respect to the equilibrium follows the following expression:

$$y(t) = A_1 e^{\lambda_1 t} + A_2 e^{\lambda_2 t} \quad where \begin{cases} \lambda_1 = \frac{-b-\sqrt{b^2-4km}}{2m} \\ \lambda_2 = \frac{-b+\sqrt{b^2-4km}}{2m} \end{cases} \tag{A.5}$$

Rewriting the expression as the equation A.3 one, this time without the phase, to simplify, we can see that:

$$y\left(t\right) = Ae^{i\omega' t} \tag{A.6}$$

$$where\ \omega\prime = i\omega_0 \left(-\zeta \pm \sqrt{\zeta^2\ -\ 1}\right) \quad and \quad \zeta = \frac{b}{2\sqrt{mk}}$$

The herein defined ζ is the so-called damping ratio and is the parameter that determines how the oscillator will behave. Now we see that depending on the value of ζ -that depend on k, m and b- we can have 3 possible situations that are ilustrated in Figure 12.

A.2.1 Overdamped harmonic oscillator ($\zeta > 1$)

This situation leads to a purely real term in the exponential. And so, the final equation results in an exponential decay to $y = 0$, i.e. to the equilibrium position. The larger the damping ratio, the slower is the return to that equilibrium position.

$$y(t) = Ae^{-|\omega'|t} \tag{A.7}$$

A.2.2 Critically damped harmonic oscillator ($\zeta = 1$)

In this case, the damping makes the system return to the equilibrium as quickly as possible, as $\omega' = -i\omega_0$ giving an exponential decay.

A.2.3 Underdamped harmonic oscillator ($\zeta < 1$)

In this last situation we will have the following expression describing the movement:

$$y(t) = Ae^{-\zeta\omega_0 t - i\omega_0\sqrt{1-\zeta^2}t} = Ae^{-\zeta\omega_0 t}e^{i\omega_0\sqrt{1-\zeta^2}t} \tag{A.8}$$

In this case we have an oscillation at a characteristic angular frequency $\omega_1 = \omega_0\sqrt{1-\zeta^2}$ but with a decreasing amplitude that returns to the equilibrium position as in the critically damped harmonic oscillator (at a decay time $\tau = \frac{1}{\zeta\omega_0}$).

A.3 Response to a force of a harmonic oscillator

In an underdamped system it is interesting to define the quality factor Q as:

$$Q = 2\pi\frac{\text{energystored}}{\text{energylostinaperiod}} = \frac{\sqrt{km}}{b} = \frac{1}{2\zeta} \tag{A.9}$$

In fact, this value is π times the number of oscillations that the system makes while its amplitude is divided by a factor e. As seen in equation A.9, Q is inversely related to the damping factor, which makes sense, because a higher damping leads to more energy losses in the system.
The previous division of damped mechanical oscillators can be also done looking at this Q factor. In this sense, overdamped oscillators have a $Q < 1/2$, critically damped ones

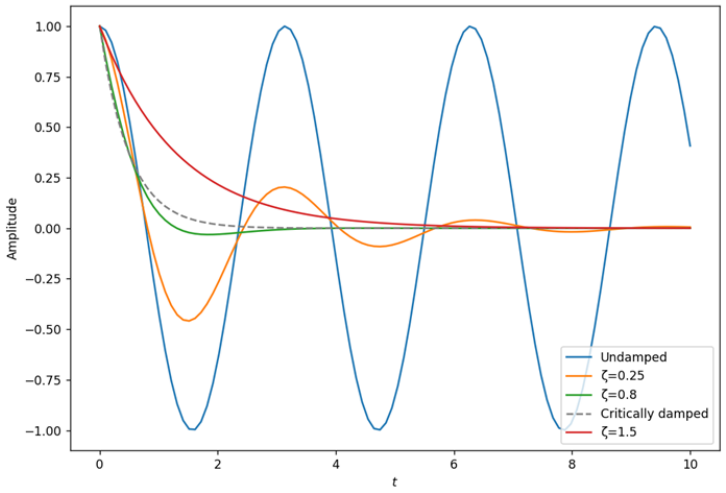

Figure 12: Response of an oscillator depending on the damping factor

a $Q = 1/2$ and undamped oscillators, $Q > 1/2$. This factor is really relevant because it describes the response of the resonator to an external force. In this case, we study how the oscillator responds to an external oscillating force. So, applying the second Newton's law again, we can see that:

$$m\frac{d^2y}{dt^2} + b\frac{dy}{dt} + ky = F_m e^{\omega t} \tag{A.10}$$

The solution for this system is the one in equation A.3, but the amplitude of the movement is

$$A = \frac{F_m}{k - m\omega^2 + ib\omega} \tag{A.11}$$

This includes an extra phase to the movement, as the amplitude has an imaginary part. To summarize all, the final expression (considering the initial phase to be 0) is:

$$y = \rho e^{i\phi} e^{i\omega t} = \rho e^{i(\omega t + \phi)} \tag{A.12}$$
$$where \begin{cases} \rho = |A| = \left|\frac{F_m}{k - m\omega^2 + ib\omega}\right| \\ \phi = \arg(A) = \arg\left(\frac{F_m}{k - m\omega^2 + ib\omega}\right) \end{cases}$$

There are two important conclusions that can be extracted from this result:

- The extra phase that appears in the oscillator is always negative, meaning that the oscillator responds belatedly to the external force.
- Rewriting the expression in terms of Q, we notice that a higher quality factor increases the amplitude of the movement. This is in accordance to the Q factor definition, which attends to the stored energy (in this case it is the sum of the potential and kinetic energies at some point in time) times the lost energy (which is the work done by the external force each cycle, to maintain amplitude).

$$A = \frac{F_m}{k} \frac{1}{1 - \left(\frac{\omega}{\omega_o}\right)^2 + i\frac{\omega}{\omega_o}\frac{1}{Q}} \tag{A.13}$$

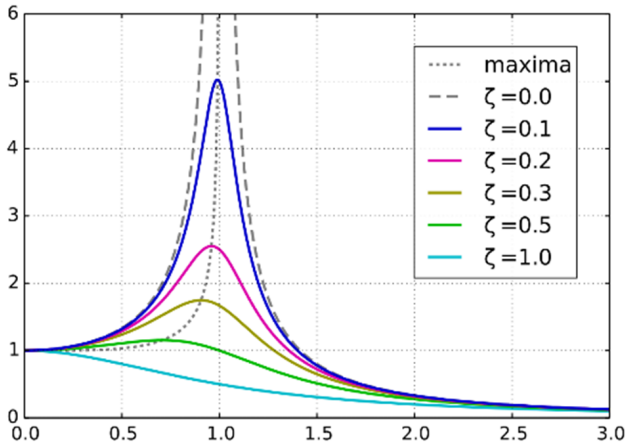

Figure 13: Response of an oscillator at different frequencies. y axis is expressed in $\frac{F_m}{k}$ units

A.3.1 Notation for mechanical resonators

Equation A.9 can also be expressed as

$$m_{eff}\frac{d^2x(t)}{dt^2} = -m_{eff}\Omega_m^2 x(t) - m_{eff}\Gamma_m\frac{d}{dt}x(t) + F(t) \tag{A.14}$$

where m_{eff}, Ω_m and Γ_m, respectively, represent the effective mass, resonance frequency (ω_o) and decay rate of the mechanical resonator. This last parameter Γ_m is related with the damping ratio as $\Gamma_m = 2\zeta\omega_o$.
And so, the response of the resonator to the external force can be expressed as in equation A.11, using the mechanical resonator parameters, in the frequency domain as follows

$$x(\omega) = \chi(\omega)F(\omega) \tag{A.15}$$

where the susceptivility $\chi(\omega)$ expression is

$$\chi(\omega) = \frac{1}{m_{eff}\left(\Omega_m^2 - \omega^2\right) - i\Gamma_m m_{eff}\omega} \tag{A.16}$$

Moreover, the response of the oscillator could be now expressed as

$$x_h(t) = A_o e^{-\Gamma_m/2} e^{i\left(\sqrt{\Omega_m^2 - \left(\frac{\Gamma_m}{2}\right)^2}t\right)} \tag{A.17}$$

And the quality factor Q as

$$Q_m = \frac{\Omega_m}{\Gamma_m} \tag{A.18}$$

B Effective mechanical frequency and damping derivation

To understand the dynamics our system undergoes, we can assume that the system makes small variations $\delta a(t)$ and $\delta x(t)$ arround the equilibrium position: $a(t) = \bar{a} + \delta a(t), x(t) = \bar{x} + \delta x(t)$. Equations 1.17 and 1.18 will result in

$$\frac{d\delta a(t)}{dt} = i(\Delta + G\bar{x})\delta a(t) - \frac{\kappa}{2}\delta a(t) + iG\bar{a}\delta x(t) \tag{B.1}$$

$$m_{eff}\frac{d^2\delta x(t)}{dt^2} = -m_{eff}\Omega_m^2\delta x(t) - m_{eff}\Gamma_m\frac{d\delta x(t)}{dt} + \hbar G\bar{a}\left(\delta a(t) + \delta a^*(t)\right) + F(t) \tag{B.2}$$

As a next step, we can Fourier transform the set of equations to obtain

$$-i\omega\delta a(\omega) = i(\Delta + G\bar{x})\delta a(\omega) - \frac{\kappa}{2}\delta a(\omega) + iG\bar{a}\delta x(\omega) \tag{B.3}$$

$$-m_{eff}\omega^2\delta x(\omega) = -m_{eff}\Omega_m^2\delta x(\omega) - im_{eff}\Gamma_m\omega\delta x(\omega) + \hbar G'\bar{a}\left(\delta a(\omega) + \delta a^*(\omega)\right) + F(\omega) \tag{B.4}$$

Obtaining

$$\delta a(\omega) = \frac{iG\bar{a}}{-i(\Delta + G\bar{x} + \omega) + \frac{\kappa}{2}}\delta x(\omega) \tag{B.5}$$

The induced intracavity energy modulation gives rise to an oscillating lightinduced force $F_{rp}(\omega) = \hbar G\bar{a}\left(\delta a(\omega) + \delta a^*(\omega)\right)$ called dynamical backaction.
On the mechanical size, the effective susceptivility $\chi_{m,eff}(\omega)$, which relates to $\delta x(\omega)$ as $\delta x(\omega) = \chi_{m,eff}(\omega)F(\omega)$ takes the form

$$\chi_{m,eff}(\omega) = \frac{1}{m_{eff}\left(\Omega_{eff}^2 - \omega^2\right) - i\omega m_{eff}\Gamma_{eff}} \tag{B.6}$$

were

$$\Omega_{\text{eff}}^2 = \Omega_m^2 + \Omega_{om}^2 = \Omega_m^2 + 2\Omega_m g_o^2|\bar{a}|^2\left(\frac{\bar{\Delta} + \Omega_m}{\left(\bar{\Delta} + \Omega_m\right)^2 + (\kappa/2)^2} + \frac{\bar{\Delta} - \Omega_m}{\left(\bar{\Delta} - \Omega_m\right)^2 + (\kappa/2)^2}\right) \tag{B.7}$$

$$\Gamma_{eff} = \Gamma_m + \Gamma_{om} = \Gamma_m + g_o^2|\bar{a}|^2\left(\frac{\kappa}{\left(\bar{\Delta} + \Omega_m\right)^2 + (\kappa/2)^2} - \frac{\kappa}{\left(\bar{\Delta} - \Omega_m\right)^2 + (\kappa/2)^2}\right) \tag{B.8}$$

C Wave propagation in ordered and disordered materials

C.1 Electrons in periodic potentials

Any crystalline material consists in a regular array of atoms arranged in a crystal lattice. The most important property of this periodicity in space is that crystals have translational invariance, meaning that displacing the crystal by one lattice constant, will end up in the same structure. In 1D this can be written as:

$$U(x+a) = U(x) \tag{C.1}$$

where a is the lattice constant of the one-dimensional lattice.
The atoms and ions of the structure create a periodic potential. This potential creates an electromagnetic field to which electrons in the material are subjected to.

C.1.1 Free electrons

If the electrons were moving in a periodic potential where $V(\vec{r}) = 0$, free electrons, we would have the following Hamiltonian.

$$-\frac{\hbar^2}{2m_0}\nabla^2\psi(\vec{r}) = E\psi(\vec{r}) \tag{C.2}$$

This free electron model gives a plane wave solution, $\psi(\mathbf{r}) = Ae^{i\mathbf{k}\cdot\mathbf{r}}$, for which the energy dispersion is $E = \frac{\hbar^2|\mathbf{k}|^2}{2m_o}$.

C.1.2 Kronig–Penney model

To illustrate the effect of the periodic potential we can look at the Kronig–Penney model. This is a simple model in which the electron is placed in an infinite 1D crystal in which the atom's potential is considered to be rectangular. The Hamiltonian of the system is then:

$$-\frac{\hbar^2}{2m_0}\nabla^2\psi(\vec{r}) + V(\vec{r})\psi(\vec{r}) = E\psi(\vec{r}) \tag{C.3}$$

$$\nabla^2\psi(\vec{r}) + \frac{2m_0}{\hbar^2}[E - V(\vec{r})]\psi(\vec{r}) = 0 \tag{C.4}$$

Bloch's theorem establishes that the wave function $\psi_{\vec{k}}(x)$ of the electron in a crystal, can be expressed as the product of a plane wave and a function with the same periodicity of the lattice $u_{\vec{k}}(x)$, called Bloch function.

$$\psi_{\vec{k}}(x) = e^{ik\cdot x}u_{\vec{k}}(x) \tag{C.5}$$

where

$$u_{\vec{k}}(x) = u_{\vec{k}}(x+a) \tag{C.6}$$

and so

$$\psi_{\vec{k}}(x+a) = e^{ika}\psi_{\vec{k}}(x) \tag{C.7}$$

Now, by solving the solution for a single period of the lattice, considering each region as having constant potential. Then, the Bloch Function $u_{\vec{k}}(x)$ can be found.

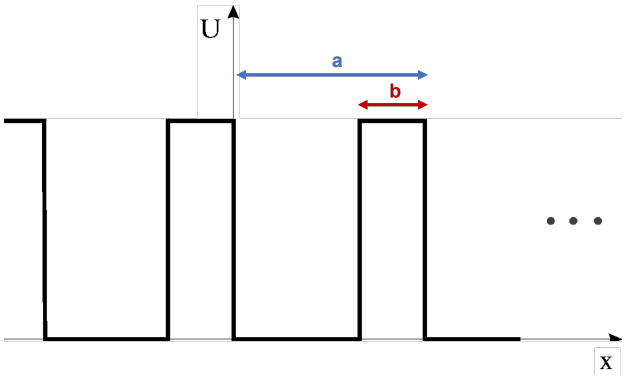

Figure 14: Schematic of the Kronig–Penney model periodic potential

Taking Figure 14 as the reference, for the $0 < x < (a - b)$ region, we have:

$$\psi(x) = Ae^{i\alpha x} + A'e^{-i\alpha x} \quad \left(where \;\; \alpha^2 = \frac{2mE}{\hbar^2}\right) \tag{C.8}$$

as this function must follow equation C.5, we have that:

$$u(x) = Ae^{i(\alpha - k)x} + A'e^{-i(\alpha + k)x} \tag{C.9}$$

And for $-b < x < 0$:

$$\psi(x) = Be^{i\beta x} + B'e^{-i\beta x} \quad \left(where \;\; \beta^2 = \frac{2m\,(E + V_0)}{\hbar^2}\right) \tag{C.10}$$

$$u(x) = Be^{i(\beta - k)x} + B'e^{-i(\beta + k)x} \tag{C.11}$$

To end up having the correct solution, we have to ensure that the wavefunction and the Bloch function are continuous, smooth and periodic.

$$\psi\left(0^-\right) = \psi\left(0^+\right) \quad \psi'\left(0^-\right) = \psi'\left(0^+\right)$$

$$u(-b) = u(a - b) \quad u'(-b) = u'(a - b)$$

If this 4 equation system is solved with a non-trivial solution we have the following relation:

$$\cos(ka) = \cos(\beta b)\cos[\alpha(a - b)] - \frac{\alpha^2 + \beta^2}{2\alpha\beta}\sin(\beta b)\sin[\alpha(a - b)]. \tag{C.12}$$

That for the case where we have a potential with infinite delta functions ($b \to 0; \quad V_0 \to \infty$) the expression simplifies like:

$$\cos(ka) = \cos(\alpha a) + \frac{mV_0 ba}{\hbar^2}\frac{\sin(\alpha a)}{\alpha a} \tag{C.13}$$

C.1.3 Band diagrams

This type of relation between E (which is inside α and β) and k gives rise to different energy dispersion relation diagrams. In Figure 15 we see the band structure of Si. We can observe a band gap in the 0-1.12 eV energy range.

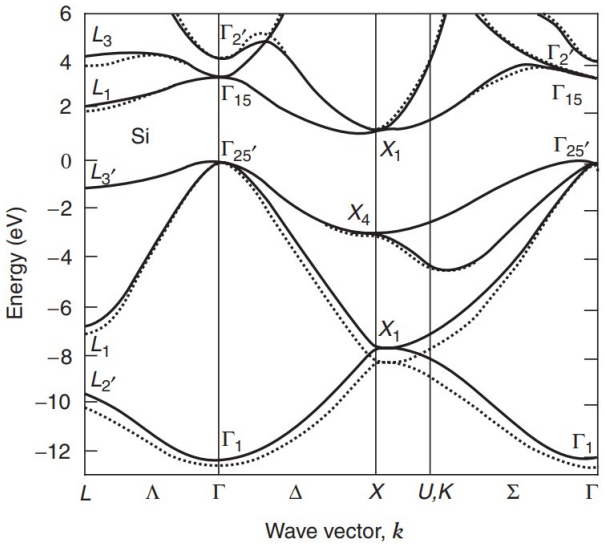

Figure 15: Band structure of Si from an empirical nonlocal (full line) or local (dotted line) pseudopotential calculation. (Reprinted figure with permission from Chelikowsky JR and Cohen ML (1976) Nonlocal pseudopotential calculations for the electronic structure of eleven diamond and zinc-blende semiconductors. Physical Review B 14: 556; American Physical Society [45])

C.2 Light in photonic crystals

C.2.1 Maxwell-Schrödinger isomorphism

C.2.1.1 Maxwell laws

During the 19th century, scientists formulated quantitative laws that related the interactions between electrical current in conductors, electric fields and magnetic fields. Some of them are the Ampère's law (1831) [46], Faraday's law (1831) [47] or Lenz's law (1834) [48]. It wasn't until 1865, when James Clerk Maxwell published 'A Dynamical Theory of the Electromagnetic Field' [49], when these laws were unified in a coherent description of the electromagnetic field. Later in 1884, Oliver Heaviside and Willard Gibbs put these equations together and reformulated them in the current vector notation. For a linear medium we have that:

$$\begin{aligned} \vec{\nabla} \cdot \overrightarrow{\mathbf{E}} &= \tfrac{\rho_f}{\epsilon} \\ \vec{\nabla} \cdot \overrightarrow{\mathbf{B}} &= 0 \\ \vec{\nabla} \times \overrightarrow{\mathbf{E}} &= -\tfrac{\partial \overrightarrow{\mathbf{B}}}{\partial t} \\ \vec{\nabla} \times \overrightarrow{\mathbf{B}} &= \mu \vec{\mathbf{J}}_f + \mu\epsilon \tfrac{\partial \overrightarrow{\mathbf{E}}}{\partial t} \end{aligned} \tag{C.14}$$

where ρ_f is the free charges density, $\vec{\mathbf{J}}_f$ the current density, μ is the permeability and ϵ the permittivity of the medium. Maxwell equations describes the electric ($\overrightarrow{\mathbf{E}}$) and magnetic field ($\overrightarrow{\mathbf{B}}$) and their changes. The first one is the Gauss Law that describes how charges affect the electric field, and so tells that free charge density are the source of displacements. The second law tells that magnetic monopoles do not exist and so the magnetic field closes on itself. The third one is the Faraday Law. That tell how the electric field will react to magnetic field changes in time. And the forth one, the Ampère-Maxwell law, tells us that the magnetic field will react to free charges moving and to a change in the electric field.

C.2.1.2 Propagation speed in an homogeneous medium

Considering a linear and homogeneous medium, in which there are no free charges, i.e., $\rho_f = 0$. From the third equation in C.14 we can extract that:

$$\begin{array}{c} \vec{\nabla} \times \left(\vec{\nabla} \times \vec{E} = -\frac{d\vec{B}}{dt}\right) \\ \vec{\nabla}(\vec{\nabla} \cdot \vec{E}) - \nabla^2 \vec{E} = -\frac{d}{dt}[\vec{\nabla} \times \vec{B}] \end{array} \tag{C.15}$$

Knowing there are no free charges, $\vec{\mathbf{J}}_f = 0$. And so, we can introduce the first and forth equations in C.14 into the equation C.15 we get that

$$\nabla^2 \vec{E} - \mu\varepsilon \frac{d^2}{dt^2} \vec{E} = 0 \tag{C.16}$$

Solving this differential equation, we see that the wave has a speed such that: $\frac{1}{v^2} = \mu\varepsilon$. Knowing that μ_0 and ϵ_0 are the vacuum permeability and permittivity, respectively, the relationship of the speed in the medium with the vacuum speed of light, c, via the refractive index, n, can be obtained as

$$n = \frac{c}{v} = \sqrt{\mu_r \varepsilon_r} \tag{C.17}$$

where $\mu_r = \frac{\mu}{\mu_0}$ and $\epsilon_r = \frac{\epsilon}{\epsilon_0}$.

C.2.1.3 Propagation speed in a non-homogeneous medium

A non-homogeneous medium can be achieved having a position-dependant refractive index. Some examples could be multilayer materials, nanostructures, dopping, etc.
Now, restoring the possible spatial dependence on ε and μ, considering them as time-independent scalars, we see that equation C.16 changes as:

$$\nabla^2 \vec{E} - \frac{n^2(\vec{r})}{c^2} \frac{d^2}{dt^2} \vec{E} = 0 \tag{C.18}$$

So, calling A the amplitude of the vector fields, with a behavior $A(\vec{r}, t) = A(\vec{r})e^{-i\omega t}$, we obtain for equation 1.21 that:

$$\nabla^2 A(\vec{r}) + \frac{n^2(\vec{r})}{c^2} \omega^2 A(\vec{r}) = 0 \tag{C.19}$$

C.2.1.4 Electromagnetism-quantum mechanics analogy

This equation above should be compared with Schrödinger's equation shown in eq. C.4 from where the identical mathematical structure is evident and a direct analogy can be done between the following terms:

	Electromagnetism	Quantum mechanics
Function	$A(\vec{r})$	$\psi(\vec{r})$
$k^2(\vec{r})$	$\lambda^2 \frac{n^2(\vec{r})}{c^2}\omega^2$	$\lambda^2 \frac{2m_0}{\hbar^2}[E - V(\vec{r})]$

Table 3: Electromagnetism-quantum mechanics analogies

where $k^2(\vec{r})$ are the so called Helmholtz functions and λ^2 are some characteristic lengths to rewrite the equations in terms of dimensionless parameters. So, in the same way electrons tend to go to regions with low potential energy (regions with a high $[E - V(\vec{r})]$ value),

photons will tend to regions with high $n^2(\vec{r})$. This last assertion is reliable to the Snell law, where a photon changes direction by a change on the refractive index. This similar phenomena is a consequence of the wave character of both entities: light and electrons. Any other entity described by a wavelike equation (phonons in solids, sound in air, water in a pond, etc.) may also present the same collection of quantum effects.

C.2.2 A taste of photonic crystals

Just as it happens with electrons in a periodic potential, the periodicity of the group index $n(\vec{r})$ in a photonic crystal can generate photonic gaps (see Figure 16). This gap depends on the ratio of the group index of the two materials and can give rise to some exotic phenomena such as:

- Slow light: regions of the diagram with $d\omega/dk \to 0$. This can be used in distributed feedback laser (DFB) lasers [50].
- Negative refraction: regions with $d\omega/dk < 0$. This property can be used to develope superlens that may allow imaging below the diffraction limit or higher nanolithography resolutions [51].
- Regions with a high curvature, i.e. a quick change in the refractive index with frequency that could allows very large angular separation [52].

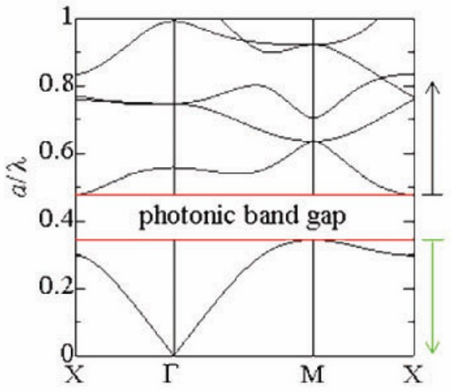

Figure 16: Band diagram of a Photonic crystal with a square pattern (from Alongkarn Chutinan, Nazir P. Kherani, Stefan Zukotynski, "High-efficiency photonic crystal solar cell architecture," Opt. Express 17, 8871-8878 (2009)) [53]

If at some point of the structure, the pattern is not followed the energy diagram will change. In the case of punctual defects, a mode can be pushed up or down in energy. This can generate a mode that is in the band gap region. The mode in that deffect will be localized and the field will be an exponential decay proportional to $\sqrt{\omega - \omega_o}$.
If we have a line defect, we could have a energy band that could be in the center of the gap if the design of the structure is the optimal. This can allow to have modes confined in that line defect. Those are also called guided modes since the frequencies of these modes are not allowed outside the gap region, i.e., they can only be able to propagate through it as they can't couple to any other band of the diagram.

C.3 Anderson Localization

Anderson Localization (AL) is a phenomena associated with any undulatory system (electromagnetic wave, quantum mechanics, acoustics, sea waves, etc.) with disorder [54].
If we consider a 1D wave propagating in space, we will see that its intensity is equal to its power ($I = P$). If we look at a 2D wave, the power of the wave is now distributed for all the perimeter, so the intensity should be $I = \frac{P}{2\pi r}$. The same happens in 3D, where the power is distributed for all the surface: $I = \frac{P}{4\pi r^2}$. A general relation can be extracted:

$$I_{nD} \propto \frac{1}{r^{n-1}} \tag{C.20}$$

where r is the distance from the emission point and n the number of dimensions. When disorder starts to play a role in the system, we can have some points where the light scatters and where it can even bounce back. This will generate positive and negative interferences that change the intensity of the wave depending on position.

C.3.1 1D Anderson Localization

We will consider emission in the $x = 0$ position in a system with impurities (scatterers). As waves with the same amplitude but random phases will start to sum up, the amplitude of the wave will exponentially decay. The result is a wave that doesn't propagate, it is localized.

$$A = A_o e^{-\frac{x}{\lambda_{loc}}} \tag{C.21}$$

where the λ_{loc} parameter is the localization length, a measurement of the size of the localized state. It could be compared with similar parameters in Quantum Mechanics, like the Bohr radius in the hydrogen atom.

C.3.2 2D and 3D Anderson Localization

In these two cases, we also sum up waves with random phases but not with the same amplitude, as from equation C.20 we see that this parameter had a distance dependance. So now, light scattered nearer to the emissor will have more importance in this localization. Amplitude will decay both for the number of dimensions and for the localization phenomena, and a λ_{loc} parameter can be extracted as well.

C.3.3 Amount of disorder vs Anderson Localization

The scatterer density has an important relevance in AL as the distance from the emission point to a scattering point is important for low dimension propagating waves. In 1D systems any disorder can produce AL, as ideally the amplitude remains constant at any position x. Nevertheless, in 2D we have a logarithmic divergence, as it has been proven that any scatterer density can also cause AL, but for higher dimensions there is a threshold under which there is not AL.
For small sistems, i.e., systems with a characteristic length smaller than the localization length ($L << \lambda_{loc}$) we won't see the effects of the localization.

C.4 Vibrations in photonic crystals

C.4.1 Phonon propagation

C.4.1.1 1D phonon propagation model

Just as in the photonic propagation, we can see the one-dimensional lattice model for phonons and make the extrapolation to multiple dimensions. In this case we have an N-atomic lattice of identical atoms equally spaced with a distance a in equilibrium and a mass m (see Figure 17). Each atom can be denoted a number $n = 1, \ldots, N$ corresponding to his position in the lattice.

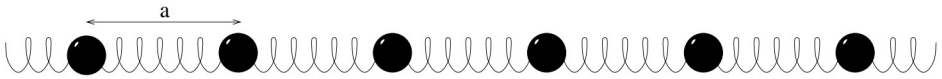

Figure 17: 1D atomic row classical model

Atoms in equilibrium are equally spaced. So, the position of the n^{th} atom can be denoted as

$$x_n = na \tag{C.22}$$

And its deviation from equilibrium is given by:

$$u_n(t) = x_n(t) - na \tag{C.23}$$

All in all, if we consider K to be the spring constant that links the atoms, we have a bunch of coupled harmonic oscillators that could be described with the following Hamiltonian:

$$H = \sum_n \frac{1}{2} m \left(\frac{du_n}{dt}\right)^2 + \frac{K}{2} \sum_n (u_n - u_{n-1})^2 \tag{C.24}$$

The equation of motion would be then:

$$m\ddot{u}_n = -\frac{\partial U_{har}}{\partial u_n} \tag{C.25}$$

$$m\ddot{u}_n = -K\left(2u_n - u_{n-1} - u_{n+1}\right) \tag{C.26}$$

If we consider periodic boundary conditions, i.e., $u_{n+N} = u_n$. The solution of eq. D.36 can be solved as:

$$u_n = Ae^{i(kna - \omega t)} \tag{C.27}$$

where

$$k = \frac{2\pi}{Na} l \quad \left(l = -\frac{N}{2}, \ldots, \frac{N}{2}\right) \tag{C.28}$$

When substituting the expression D.37 in D.36, we have

$$m\omega^2 = K\left(2 - e^{ika} - e^{-ika}\right) = 4K \sin^2\left(\frac{ka}{2}\right) \tag{C.29}$$

and so, the dispersion relation is:

$$\omega = 2\sqrt{\frac{K}{m}} \left|\sin\left(\frac{ka}{2}\right)\right| \tag{C.30}$$

C.4.1.2 1D phonon propagation model in a periodic medium

In the previous cases a periodicity in the potential or the refractive index could give rise to different bands and result in band gaps where some frequencies are not allowed. In this case, what will produce this effect will be the periodicity in the spring constant between the atoms, i.e., a periodic change of the elastic modulus of the material.
A quick demonstration of the emergence of band gaps is the dimerization of the lattice. Considering a system of atoms of the same mass m, but joined with springs of different spring constant K and G. W will now have two types of atoms per cell (herein called type-1 and type-2). The potential energy of the system will be:

$$U_{har} = \frac{K}{2}\sum_{n=1}^{N}(u_{1n} - u_{2n})^2 + \frac{G}{2}\sum_{n=1}^{N}(u_{2n} - u_{2,n+1})^2 \tag{C.31}$$

Proceeding as in the previous section, we see that:

$$\begin{aligned} u_{1n} &= A_1 e^{i(kna-\omega t)} \\ u_{2n} &= A_2 e^{i(kna-\omega t)} \end{aligned} \tag{C.32}$$

And the energy dispersion relation is:

$$\omega^2 = \frac{K+G}{M} \pm \frac{1}{M}\sqrt{K^2 + G^2 + 2KG\cos(qa)} \tag{C.33}$$

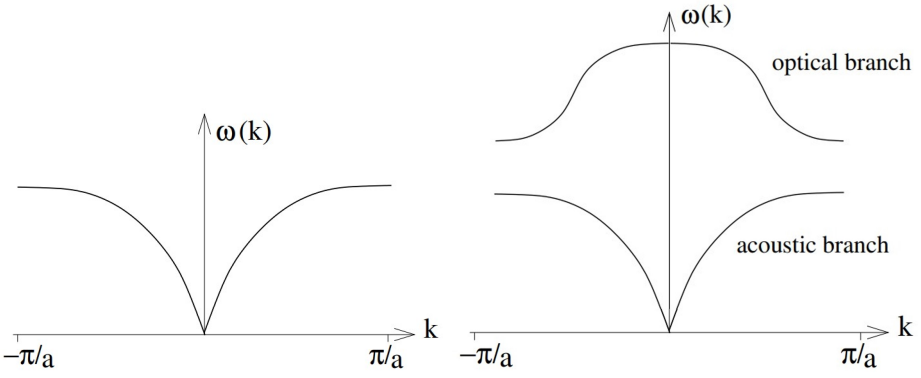

Figure 18: Right: phonon dispersion relation for a monatomic chain. Left: phonon dispersion relation for a diatomic chain.

C.4.2 Phononic crystals (PC)

Just as in photons, arranging periodically different materials with different elastic constant can produce phenomena like phononic gaps or slow sound. A proper design can also lead to the creation of localized and guided modes which can also have different applications [55].

D Mechanical motion detection

In the setup, mechanical motion is detected by measuring the transmitted light with a high frequency photoreceiver.
Given a detuning $\Delta = \omega_\ell - (\omega_o - Gx(t)) \equiv \Delta_0 + Gx(t)$. we can aproximate the transmittance as

$$T(t,\Delta) = T(\Delta_0) + \left.\frac{dT}{d\Delta}\right|_{\Delta=\Delta_o} \frac{d\Delta}{dx(t)} x(t) = T(\Delta) + \frac{dT}{d\Delta} Gx(t) \tag{D.34}$$

where we have considered that there is no backaction of the light field on the mechanical motion. The transmission derivative with respect to the detuning is:

$$\frac{dT}{d\Delta} = \frac{\Delta\kappa_e\left(\kappa - \frac{\kappa_e}{2}\right)}{\left(\Delta^2 + \left(\frac{\kappa}{2}\right)^2\right)^2} \tag{D.35}$$

Figure 19 diagramatically shows the mechanism to detect mechanical motion and plots the derivative $\frac{dT}{d\Delta}$. The transduction of this mechanical motion has two maxima and is null at the resonance ($\Delta = 0$).

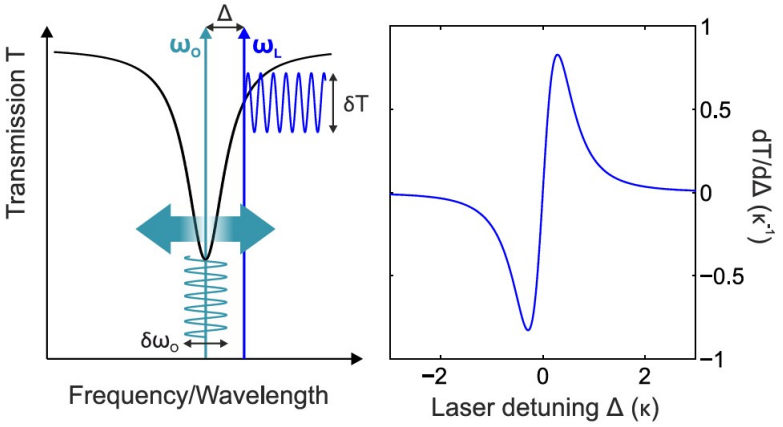

Figure 19: Optomechanical transduction of motion scheme (Reprinted figure from "Light-motion interaction in disordered nanostructures" Artegui, Guillermo (2021) [28])

The total modulated power we expect from a mechanical motion $x(t)$ is

$$P_m(t) = P_{in}\frac{dT}{d\Delta} Gx(t) = 2\hbar\omega_\ell G\left|a_{in}\right|^2 \frac{\Delta\kappa_e\left(\kappa - \frac{\kappa_e}{2}\right)}{\left(\Delta^2 + \left(\frac{\kappa}{2}\right)^2\right)^2} x(t) \tag{D.36}$$

The optical power $P_m(t)$ is measured on a photodetector, leading to a voltage $V_m(t) = \eta_{det} G_{det} P_m(t)$, where we have introduced the detector efficiency η_{det} and its transimpedance gain G_{det}. The photodetector signal is then fed to an electronic spectrum analyzer (ESA), which measures the electrical power $P_e = \langle V_m(\omega)^2\rangle / R$, with R the characteristic impedance of the detector. The measured signal is therefore

$$P_{ESA}(\omega) = 2\left(\frac{\eta_{det} G_{det}}{\sqrt{R}}\right)^2 G^2\hbar\omega_\ell\left|a_{in}\right|^4\left(\frac{dT}{d\Delta}\right)^2\left\langle x(\omega)^2\right\rangle \tag{D.37}$$

from which the power spectral density can be extracted.

E Group velocity and Anderson Localized modes of the sample

For wavelengths between 1460 nm and 1485 nm, the spectral position of the dips are periodic in wavelength. These dips are manifestations of the Fabry-Pérot modes of the optical cavity. At higher wavelengths the location of the transmission dips is not regular. This is a regime of Anderson-localization and the dips will depend on the position of the air slot where the measurement is taken.
The localization phenomenon in that wavelength range derives from the slow light regime presented by the device. The optical band structure flattens near the Brillouin Zone edge. Group velocity can be obtained from the band diagram of a system, via the following relation:

$$v_g = \frac{\partial \omega}{\partial k} \tag{E.38}$$

So, the flatter the ω vs k dispersion relation, the slower the light. In a Fabry-Pérot cavity, the group index can be extracted from the frequency difference between the characteristic modes following the following relation:

$$\mathrm{n}_g = \frac{\mathrm{c}}{2\Delta v_{FSR} L} \tag{E.39}$$

where n_g is the group index, c is the speed of light, Δv_{FSR} is the free spectral range, and L the length of the cavity.

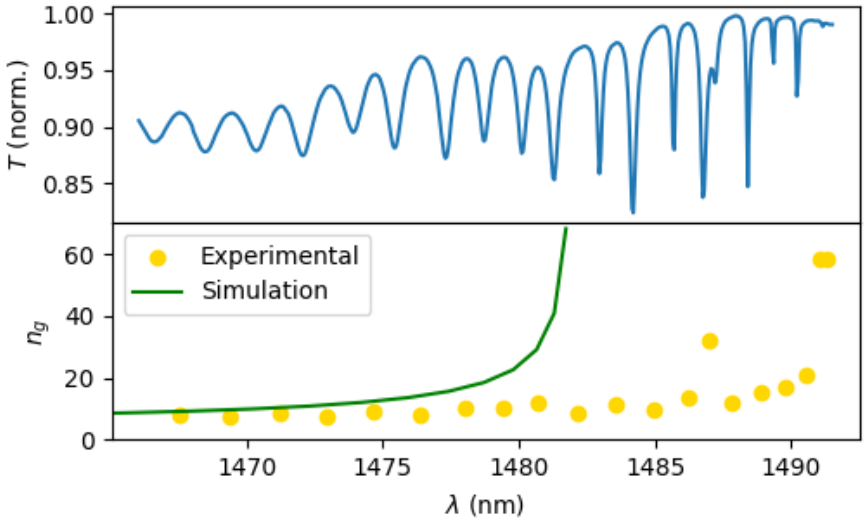

Figure 20: Top: Low P_L (<0.2mW) transmission spectra. Bottom: Comparison of the experimental and numerical group index

The group index is the relation between the speed of light in vacuum and the group velocity: $\mathrm{n_g} = \mathrm{c}/\mathrm{v_g}$. Figure 20 compares both the theoretical (from the band diagram presented in [35]) and the experimental group index (using equation E.39). The experimental and theoretical group index seem to be shifted from one-another by a wavelength of 5 nm. This mismatch can be explained considering the nanofabrication errors. Both experimental and theoretical group index calculations were done taking the original design length

L. Ideally, the cavity length of the platform should be the same as in the design one, but a difference of several nanometers can slightly change the properties of the sample.
Results seem to be in accordance until reaching the aforementioned localized region, where Fabry-Pérot modes are still present but are not the only visible modes in the transmission spectrum as dips corresponding to the localized modes are also present.
In this regime of slow light, electromagnetic waves interact more strongly with the medium making it more sensitive to the nanoscale roughness. As light-matter interactions increase, some of the wavelengths can experience positive interferences when scattering on those nanofabrication imperfections giving rise to localized modes that do not spatially span the length of the entire cavity.
Few AL modes appear in this low power measurement comparing it with the Figure shown in [35] where the average spectrum seems to show the presence of several of them. This is again a remarkable influence on the position where the measurement is taken. As it is performed at low powers, the evanescent field of the fiber will only be able to couple to the optical modes in the proving point.

F Extra figures

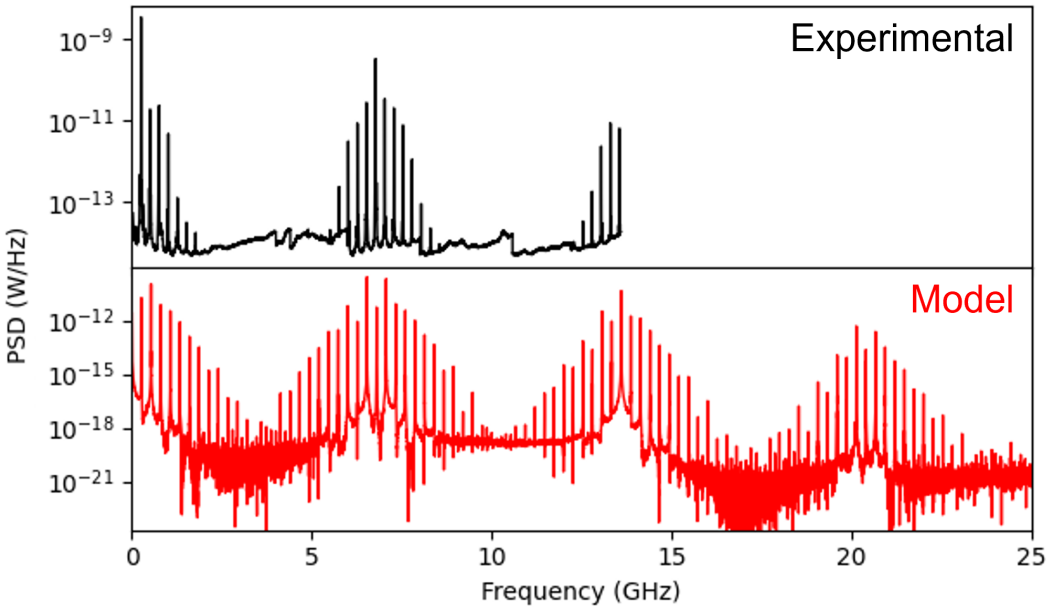

Figure 21: Top: full ESA range for the Comb regime. Bottom: FFT mot the model result in the same regime

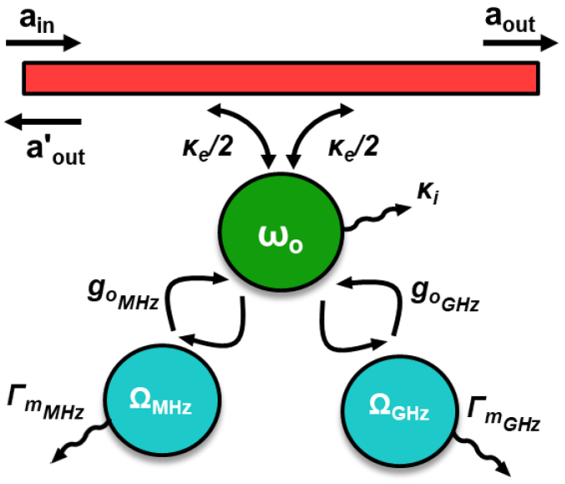

Figure 22: Schematic of the M-O-M coupling

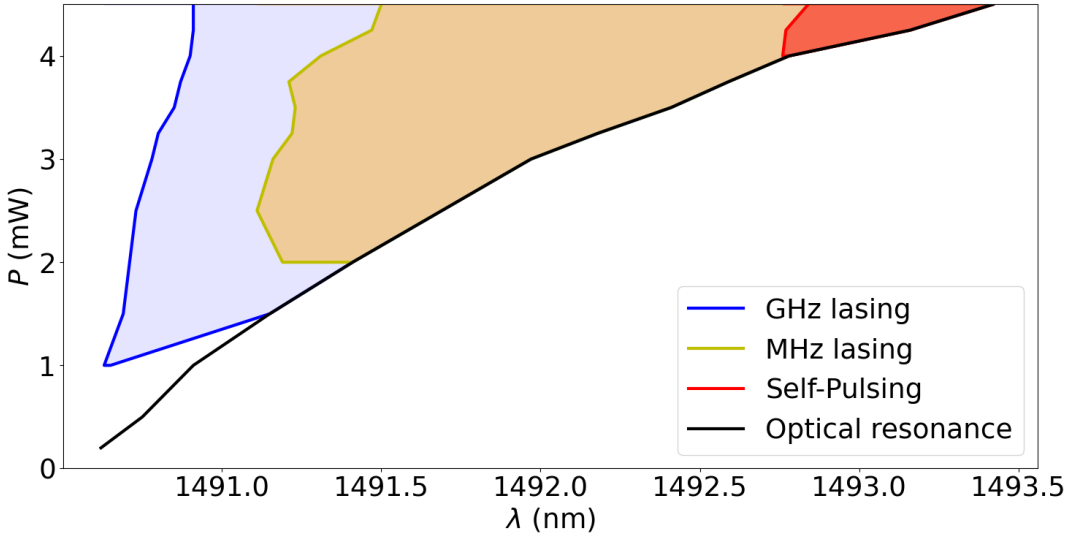

Figure 23: Color map showing the different regimes of the system. Dark line shows the optical resonance wavelength shifted by the TO effect. Blue and yellow lines show the P_{th} of the GHz and MHz modes respectively. Red line the input power for which the SP is activated. Coloured regions correspond to SML (blue), Comb (orange) and Comb + SP (red).